The Astrophysical Journal, 895:69 (18pp), 2020 May 20 https://doi.org/10.3847/1538-4357/ab8ea7

Milky Way Subsystems from Globular Cluster Kinematics Using Gaia DR2 and HST Data

A. T. Bajkova[1], G. Carraro[2], V. I Korchagin[3], N. O. Budanova[3], and V. V. Bobylev[1]
[1] Pulkovo Astronomical Observatory, St. Petersburg, Russia
[2] Dipartimento di Fisica e Astronomia, Universitá di Padova, Vicolo Osservatorio 3, I-35122 Padova, Italy; giovanni.carraro@unipd.it
[3] Southern Federal University, Rostov-on-Don, Russia
Received 2019 August 18; revised 2020 April 27; accepted 2020 April 28; published 2020 May 27

Abstract

We employ Gaia DR2 proper motions for 151 Milky Way globular clusters (GCs) from Vasiliev in tandem with distances and line-of-sight velocities to derive their kinematical properties. To assign clusters to the Milky Way thick disk, bulge, and halo, we follow the approach of Posti et al., who distinguished among different Galactic stellar components using stars' orbits. In particular, we use the ratio L_z/e, the Z projection of the angular momentum to the eccentricity, as a population tracer, which we complement with chemical abundances extracted from the literature and Monte Carlo simulations. We find that 20 GCs belong to the bar/bulge of the Milky Way, 35 exhibit disk properties, and 96 are members of the halo. Moreover, we find that halo GCs have close to zero rotational velocity with an average value $\langle\Theta\rangle = 1 \pm 4\,\mathrm{km\,s^{-1}}$. On the other hand, the sample of clusters that belong to the thick disk possess a significant rotation with average rotational velocity $179 \pm 6\,\mathrm{km\,s^{-1}}$. The 20 GCs orbiting within the bar/bulge region of the Milky Way have an average rotational velocity of $49 \pm 11\,\mathrm{km\,s^{-1}}$.

Unified Astronomy Thesaurus concepts: Milky Way Galaxy (1054); Globular star clusters (656); Milky Way dynamics (1051); Milky Way rotation (1059)

1. Introduction

The study of kinematical properties of the Milky Way globular clusters (GCs) has a long tradition. One of the most important steps in understanding the nature of the GC system was done by Zinn (1993), who suggested a cluster classification based on the horizontal branch morphology and chemical abundances. Zinn (1993) found that the metal-rich GCs ([Fe/H] > -0.8) are confined to the bar/bulge and to the disk of the Galaxy, while the metal-poor GCs ([Fe/H] $\leqslant -0.8$) are generally located in the Galactic halo. Later on, Mackey & Gilmore (2004) used Zinn's (1993) classification and compared the cluster properties with those in the Large and Small Magellanic Clouds, concluding that all young GCs and 15%–17% of the old ones are of external origin.

More recent progresses in understanding the structural properties of the Milky Way come from the Gaia space mission. The recently released Gaia DR2 catalog (Gaia Collaboration et al. 2018) allowed us to make significant progress in understanding the nature and the origin of the Milky Way GC system. The Gaia Collaboration (Gaia Collaboration et al. 2018) determined proper motions of 75 GCs. In the subsequent paper Posti & Helmi (2019) used the Gaia Data Release 2 proper-motion catalog of 75 GCs and measurements of the proper motions of another 20 distant clusters obtained with the Hubble Space Telescope (HST) and determined the kinematical properties of the GCs in the Milky Way. Posti & Helmi (2019) followed up an earlier work by Binney & Wong (2017) and described the population of the Milky Way GCs by the two-component distribution function that describes a flat, rotating disk and a spherical extended halo. Compared to the paper of Binney & Wong (2017), Posti & Helmi (2019) used a larger data set and varied the mass of the dark matter halo and its shape. Vasiliev (2019) published the proper-motion catalog of 151 Milky Way GCs with estimated uncertainties smaller than 0.1 mas $\mathrm{yr^{-1}}$ for most objects. The catalog of Vasiliev (2019) complements the measurements provided by the Gaia Collaboration (Gaia Collaboration et al. 2018) and HST-based determinations (Sohn et al. 2018) and is in excellent agreement with both.

Vasiliev (2019) compared his results with the ground-based measurements and found that they not only are much less precise than the space-based ones but also often deviate from the space-based determinations by a far larger amount than implied by the quoted uncertainties. Combining proper-motion measurements with the distance and line-of-sight velocity measurements from the literature, Vasiliev (2019) found that within the inner 10 kpc the population of the GCs has a mean rotational velocity of 50–80 $\mathrm{km\,s^{-1}}$ with nearly isotropic velocity dispersion about 100–120 $\mathrm{km\,s^{-1}}$.

Baumgardt et al. (2019) rederived the mean proper motions and space velocities for 154 Milky Way GCs using a combination of the Gaia DR2 proper motions and ground-based line-of-sight velocities of individual member stars. Mean proper motions of Baumgardt et al. (2019) are in good agreement with measurements of the Gaia Collaboration (Gaia Collaboration et al. 2018) and with Vasiliev's (2019) measurements, and they also are in good agreement with the proper motions derived by Sohn et al. (2018) from HST data if the systematic error of 0.10 mas $\mathrm{yr^{-1}}$ in the Gaia proper motions is taken into account.

Good-quality kinematical data of nearly all known GCs of the Milky Way allow one to address the problem of assigning them to different Milky Way components. A number of recent papers have been devoted to the problem of classification of GCs and the understanding of their origin (Massari et al. 2019; Myeong et al. 2019; Piatti 2019; Forbes 2020; Horta et al. 2020).

The investigation of Massari et al. (2019) is particularly relevant here. This work essentially provides a solution to the problems of the separation of GCs into the subsystems of the Galaxy and, most importantly, answers the question about the

origin of the halo GCs. To separate the GCs between internal (in situ) and external (ex situ), the authors use various dynamical properties, namely, orbital parameters like the apocenter (apo), maximum height from the disk ($Z_{\max}$), and the orbital circularity parameter Circ. The latter parameter is defined as $\mathrm{Circ} = L_z/L_z^{\mathrm{circ}}$, where L_z is the Z-component of the angular momentum of the cluster and L_z^{circ} is the angular momentum of the cluster placed on the circular orbit with the same total energy. Combination of these three parameters with the age–metallicity relation allowed us to solve the problem of the separation.

In this paper we readdress the problem of defining GCs' membership to different Milky Way components, the bar/bulge, the disk, and the halo, only on the basis of the dynamical properties of the clusters. Based on the clusters' orbit parameters such as apo and $Z_{\max}$, we first select those clusters that belong to the bar/bulge of the Milky Way and to its halo similar to how Massari et al. (2019) did. To separate the GCs within the thick-disk region of the Milky Way into the disk and halo fractions, we use instead of the circular parameter Circ the distribution of the clusters on the ratio of the Z projection of the angular momentum of the clusters to their eccentricity e, L_z/e, and demonstrate that this quantity allows us to distinguish clusters that belong to the halo and to the thick disk effectively.

In detail, the goal of this paper is to study the properties of the GC subsystems based on the dynamical properties of their orbital parameters and to test the proposed criterion using accepted models of the Galactic potential.

The paper is organized as follows. In Section 2 we describe available kinematical data and derive spatial velocity components of the GCs in the Galactocentric coordinate system. In this section we also describe the Galactic potential models (both axisymmetric and barred ones) and perform orbit integration of the clusters. Section 3 is devoted to a new method for separating GCs into Galactic subsystems, an analysis of the kinematic characteristics of the resulting subsystems, and a comparison of our results with the results of Massari et al. (2019). Section 4 is devoted to testing the separation algorithm against different potential models. Section 5 discusses results of the separation in a barred potential with different bar rotational velocities. In Section 6 we add metallicity properties of the GCs to support our findings. Finally, Section 7 summarizes our main results. The Appendix contains several tables with clusters' orbital parameters.

2. Galactic Potential Model and GCs' Orbits

GCs are distributed over a wide range of distances. To integrate their orbits, one needs therefore a model of the Milky Way potential reliable in a wide range of distances from the Galactic center out to the very distant halo. Bajkova & Bobylev (2016, 2017) specified the parameters of a few models of the Milky Way. They assumed that the potentials of the disk and of the bulge are described by the Miyamoto & Nagai (1975) and the Plummer models (Plummer 1911), respectively, while for the halo potential they adopted the models of Allen & Santillan (1991), Wilkinson & Evans (1999), and Navarro et al. (1997), the spherical logarithmic potential of Binney (Binney & Tremaine 1987), the Plummer sphere (Plummer 1911), and the Hernquist (1990) potential. To fix the parameters of the models, Bajkova & Bobylev (2016, 2017) used observational data, covering Galactocentric distances up to 200 kpc. Within 20 kpc, Bajkova and Bobylev additionally constrained the models by the line-of-sight velocities of the molecular clouds in their tangential points and by the kinematical data for 130 masers with known trigonometric parallaxes. At larger distances, Bajkova & Bobylev (2016, 2017) took into account the rotational velocities of the objects taken from the catalog of Bhattacharjee et al. (2014). Adjustment of the parameters of the Galactic potential was done also by taking into account the local density of the Galactic disk $\rho_\odot = 0.1\,M_\odot\,\mathrm{pc}^{-3}$ and the value of the force per unit mass perpendicular to the Galactic plane $K_{z=1.1}/2\pi G = 77\,M_\odot\,\mathrm{pc}^{-2}$. Bajkova & Bobylev (2016, 2017) find that the Navarro–Frenk–White (NFW) model of Navarro et al. (1997) gives the smallest residuals in the least-squares fit of the rotation curve of the Galaxy. Therefore, we use the NFW model, modified by Bajkova & Bobylev (2016, 2017), of the Galactic potential to integrate the orbits of the GCs. We refer to this potential with the acronym NFWBB.

The axisymmetric gravitational potential of the Galaxy is a superposition of the potentials of the three main components: the central spherical bulge, $\Phi_b(r(R, Z))$, the disk, $\Phi_d(r(R, Z))$, and the spherical halo, $\Phi_h(r(R, Z))$:

$$\Phi(R, Z) = \Phi_b(r(R, Z)) + \Phi_d(r(R, Z)) + \Phi_h(r(R, Z)), \quad (1)$$

with the potentials given by the expressions

$$\Phi_b(r) = -\frac{M_b}{(r^2 + b_b^2)^{1/2}}, \quad (2)$$

$$\Phi_d(R, Z) = -\frac{M_d}{[R^2 + (a_d + \sqrt{Z^2 + b_d^2})^2]^{1/2}}. \quad (3)$$

The halo potential is described by the NFW model:

$$\Phi_h(r) = -\frac{M_h}{r}\ln\left(1 + \frac{r}{a_h}\right). \quad (4)$$

In Equations (2)–(4), M_b, M_d, M_h are the masses of the subsystems, and a, b are the parameters determining the spatial density distributions in the bulge, in the disk, and in the halo of the Milky Way. Here r is the Galactocentric radius, and X, Y, Z are the Cartesian coordinates, with X-axis directed from the Galactic center toward the Sun, Y-axis in the direction of the Galactic rotation, and Z-axis directed perpendicular to the Galactic plane toward the north Galactic pole, $R^2 = X^2 + Y^2$, $r^2 = R^2 + Z^2$.

Table 1 lists the values of the best-fit parameters of the Galactic potential model, described by Equations (1)–(4). We assume that the distance of the Sun to the center of the Galaxy is $R_0 = 8.3$ kpc and the velocity of the LSR is $V_\odot = 244\,\mathrm{km\,s^{-1}}$ in accordance with Bajkova & Bobylev (2016, 2017). The peculiar velocity of the Sun relative to the local standard of rest (LSR) is taken from Schönrich et al. (2010): $(u_\odot, v_\odot, w_\odot) = (-11.1, 12.2, 7.3)\ \mathrm{km\,s^{-1}}$.

With the gravitational constant equal to unity ($G = 1$), and with the unit of length equal to 1 kpc, the parameters of the Galactic potential model, listed in Table 1, are given in units of $100\,\mathrm{km^2\,s^{-2}}$ for the potential, and for the mass in units of $2.325 \times 10^7\,M_\odot$.

The axisymmetric potential was also used in the model including the Galactic bar, where, however, the bulge mass M_b is reduced by the mass of the bar, to conserve mass.

Table 1
Parameters of the Galactic Potential Model

Parameter	Value
M_b (M_{gal})	443 ± 27
M_d (M_{gal})	2798 ± 84
M_h (M_{gal})	12,474 ± 3289
b_b (kpc)	0.2672 ± 0.0090
a_d (kpc)	4.40 ± 0.73
b_d (kpc)	0.3084 ± 0.0050
a_h (kpc)	7.7 ± 2.1
M_{bar} (M_{gal})	431
Ω_{bar}, (km s^{-1} kpc^{-1})	31, 41, 55, 70
q_{bar}(kpc)	8.0
θ_{bar} (deg)	45
a_{bar}/b_{bar}	2.381
a_{bar}/c_{bar}	3.03

We adopted a triaxial ellipsoid model following Palouš et al. (1993):

$$\Phi_{bar}(R, Z, \theta) = -\frac{M_{bar}}{(q_{bar}^2 + X^2 + [Y \cdot a_{bar}/b_{bar}]^2 + [Z \cdot a_{bar}/c_{bar}]^2)^{1/2}}, \quad (5)$$

where M_{bar} is the mass of the bar, which is equal to 431 × M_{gal} ($1.0 \times 10^{10} M_{\odot}$); a_{bar}, b_{bar}, and c_{bar} are the three semiaxes of the bar ($a_{bar}/b_{bar} = 2.381$, $a_{bar}/c_{bar} = 3.03$); q_{bar} is the length of the bar; $X = R\cos\vartheta$ and $Y = R\sin\vartheta$, where $\vartheta = \theta - \Omega_{bar} \cdot t - \theta_{bar}$, Ω_{bar} is the circular velocity of the bar, t is time, and θ_{bar} is the bar orientation angle relative to Galactic axes X, Y, which is counted from the line connecting the Sun and the Galactic center (the X-axis) to the major axis of the bar in the direction of Galactic rotation. We adopted the estimates of the bar rotation velocity $\Omega_{bar} = 31$ and 41 km s^{-1} kpc^{-1} from Sanders et al. (2019), 55 km s^{-1} kpc^{-1} from Antoja et al. (2014) , and 70 km s^{-1} kpc^{-1} from Debattista et al. (2002). On the other hand, the parameters $q_{bar} = 8$ kpc and $\theta_{bar} = 45°$ from Bobylev & Bajkova (2016). All these bar parameters are listed in Table 1.

Vasiliev (2019) used Gaia DR2 measurements and determined the proper motions for 151 GCs, containing almost all known objects. Vasiliev (2019) compared also his measurements with the existing proper-motion catalogs and found a good agreement of his data with the Gaia Collaboration (Gaia Collaboration et al. 2018) and with the HST (Sohn et al. 2018) measurements. In our study we use therefore proper-motion measurements from the Vasiliev (2019) catalog. Combining Vasiliev's (2019) proper motions of the GCs with the distances and the line-of-sight velocities from Harris (2010), one can calculate the spatial velocities and the coordinates of the GCs in the Cartesian coordinate system centered on the Sun.

The knowledge of the current positions and of the velocities of the clusters, together with the potential of the Milky Way, allows us to determine clusters' orbits. We integrate the orbits backward in time for 5 Gyr. Orbit integration is carried out by the Runge–Kutta algorithm of 4 orders.

For the sake of illustration, Figure 1 shows the orbits of three clusters, NGC 6440, NGC 6838, and NGC 5824, that belong to the bar/bulge, disk, and halo of the Milky Way, respectively. The orbits shown are calculated in both the axisymmetric and barred NFWBB potentials.

The parameters of all 151 GCs calculated in the NFWBB axisymmetric potential (the initial Cartesian coordinates X, Y, and Z; the radial Π, tangential Θ, vertical W velocities; orbit parameters: the eccentricity e, the maximal orbit values Z_{max}, R_{max}, r_{max}, the Z-coordinate of the angular momentum L_z, and the total energy E) are given in Table A1 of the Appendix. In the last column, the identifier of the GC membership to either a bar/bulge (B), or a thick disk (D), or a halo (H), obtained as a result of applying our subsystem separation algorithm, is given. The orbital parameter e and the limits of variation of the L_z, as well as its mean value, obtained in a barred NFWBB potential are given in Table A2 of the Appendix.

3. Criteria of Separation and Kinematical Properties of GCs' Subsystems

Binney & Wong (2017) described the Milky Way GCs' system using a two-component distribution function. The distribution function contains eight parameters that should be fixed using available observational data. Posti & Helmi (2019) applied this approach to a sample of 75 GCs from the Gaia DR2 catalog together with 20 GCs observed with the HST. Posti & Helmi (2019) found that the halo of the Milky Way is not rotating significantly, or even has a small retrograde rotation, while the Milky Way disk rotates with a velocity of about 210 km s^{-1} at solar radius. Vasiliev (2019) used a similar approach and described the population of the GCs with a single distribution function. Vasiliev (2019) found that within 10 kpc from the center of the Galaxy the population of GCs has a mean rotational velocity of about 50–80 km s^{-1} and a nearly isotropic velocity dispersion of about 100–120 km s^{-1}. We use a different approach to assign GCs to the various components of the Milky Way. Namely, we follow the idea of Posti et al. (2018), who used stars' orbits to determine their membership to the Milky Way subsystems.

3.1. Our Separation Approach

Our approach is based on the orbital parameters of the clusters. Intuitively, clusters with elongated orbits, or having orbits highly inclined to the plane of the Galactic disk, belong to the Milky Way halo, while clusters with nearly circular orbits and high circular velocities that are close to the plane are members of the Galactic disk.

The determination of GCs as members of the bar/bulge, the disk, and the halo was done in two steps.

First, clusters probably belonging to the bar/bulge and to the halo subsystems of the Galaxy were selected. To this aim, we used the empirical stellar map of the bar/bulge region of the Milky Way taken from Wegg & Gerhard (2013). They measured the three-dimensional stellar density distribution of the galactic bar/bulge region covering an area of $|X| \times |Y| \times |Z| = 2.2 \times 1.3 \times 1.1$ kpc in the inner region of the Milky Way. This density map shows a highly elongated bar with the projected axis ratios of (1:2.1) for isophotes reaching ∼2 kpc along the major axis. GCs belonging to the bar/bulge region would need to be searched for among those located inside a volume of (±2.2) × (±1.3) × (±1.1) kpc. To refine the definition, we then add the criterion $r_{max} < 3.5$ kpc. The halo GCs were selected using as a criterion the height above the Galactic plane $|Z| > 6$ kpc, assuming that the thick-disk/halo separation occurs at $|Z|$ less than 6 kpc. The

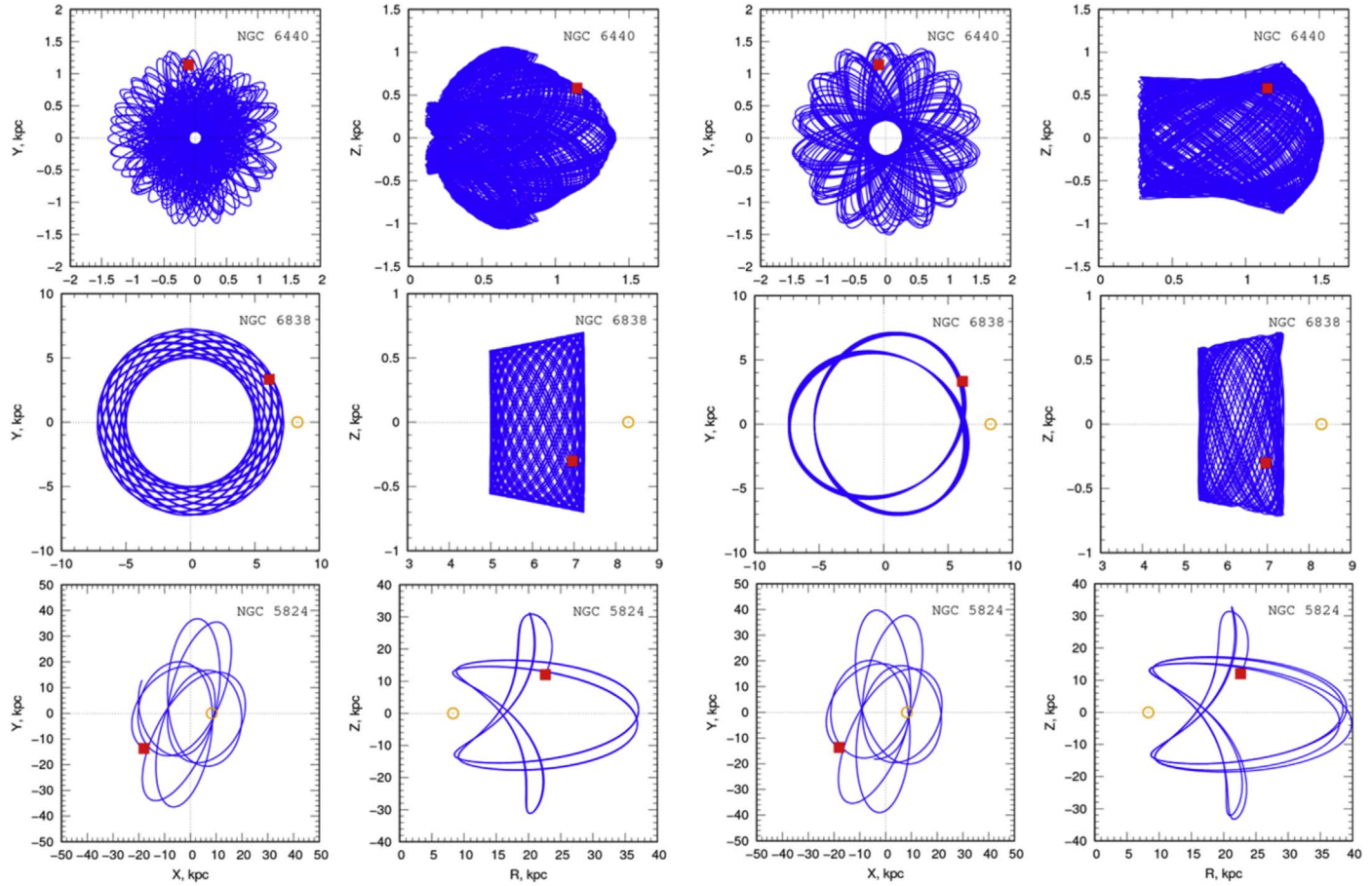

Figure 1. Orbits of NGC 6440 (top line), NGC 6838 (middle line), and NGC 5824 (bottom line) belonging to the bar/bulge, the thick disk, and the halo, respectively, obtained in the axisymmetric potential (left two columns) and in a barred potential with parameters from Table 1 (right two columns).

resulting sample of bar/bulge objects consists of 20 GCs (namely, NGC 6266, NGC 6316, NGC 6355, NGC 6440, NGC 6522, NGC 6528, NGC 6558, NGC 6624, NGC 6642, Terzan 2, Terzan 4, Terzan 1, Terzan 5, Terzan 6, Terzan 9, BH 229, Liller 1, Djorg 2, ESO 456-78, Pismis 26). The number of GCs that belong to the halo is instead equal to 56, and the number of clusters that are left out from these criteria and then would require further separation is equal to 75.

Second, the sorting of the remaining GCs was done using the probabilistic approach. The approach is based on the determination of the kinematical parameter of a GC sample that clearly demonstrates a net bimodality in their distribution within the thick disk of the Milky Way consisting of the two different classes of objects. Namely, GCs belonging to the thick disk have quasi-circular orbits with relatively small eccentricities and large circular velocities, while GCs that belong to the halo subsystem have more elongated orbits with lower circular velocities.

To split the two classes of the GCs within the thick disk of the Milky Way, we use the ratio of the angular momentum L_z to the eccentricity e. The distribution of clusters' parameter $L_z/e = \Theta \times R/e$ shows a clear bimodality. Figure 2 illustrates the approach. The left panel of the figure shows the distribution of the GCs when we adopt the axisymmetric NFWBB model of the Galactic potential. Knowing the parameters of the Gaussian distribution functions in Figure 2, which are listed in Table 2, one can determine the membership probability of a particular GC to the halo or to the disk of the Milky Way. We find that GCs belonging to the thick disk of the Milky Way consist of 35 objects (NGC 104, NGC 4372, NGC 5927, NGC 6218, NGC 6235, NGC 6254, NGC 6304, NGC 6356, NGC 6352, NGC 6366, NGC 6362, NGC 6397, NGC 6496, NGC 6539, NGC 6540, NGC 6541, NGC 6553, NGC 6569, NGC 6656, NGC 6749, NGC 6752, NGC 6760, NGC 6838, NGC 7078, Pal 1, Pal 7, Pal 8, Pal 10, Pal 11, E3, ESO 224-8, FSR 1716, BH 184, Terzan 3, Terzan 12). The number of the halo GCs within the thick disk of the Milky Way that kinematically belong to the halo is equal to 39. Combining these GCs with the clusters that are located in the Milky Way halo, we get in total 96 GCs in the Milky Way halo. We underline that a close look at individual orbits of the clusters confirms that the splitting of the clusters was done consistently.

The membership of individual GCs to a given Galaxy subsystem (GS) (B (bar/bulge), D (disk), or H (halo)) is indicated in the last column of Table A1.

3.2. Kinematical Properties of Milky Way Components as Traced by Their GCs

In this section we used the derived clusters' orbital parameters to determine the kinematical properties of the parent Galactic component. To this aim, we first characterize the uncertainties in distances, proper motions, and line-of-sight velocities by employing a Monte Carlo approach. The artificial data sets were pulled for the bar/bulge, the disk, and the halo

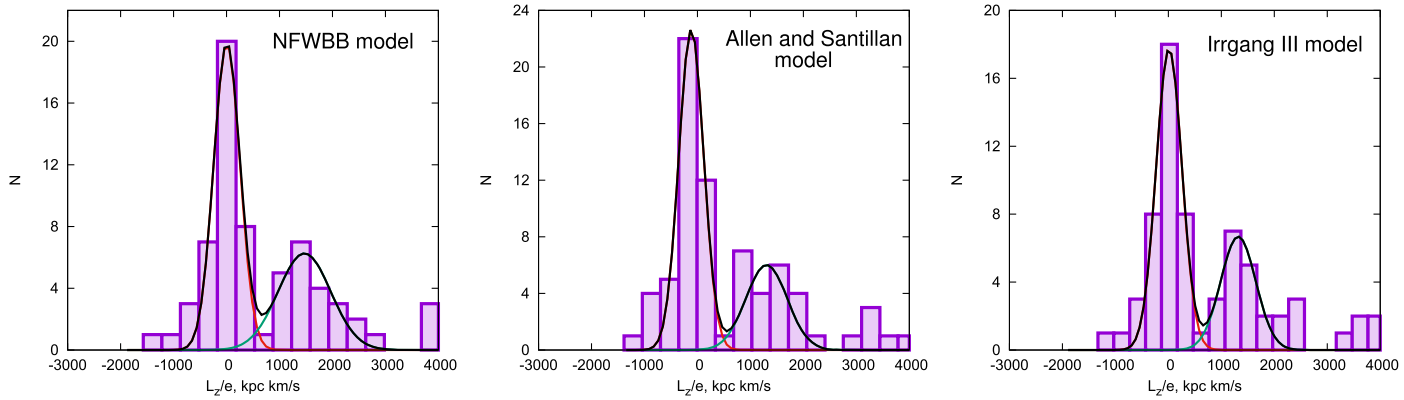

Figure 2. Distribution of the GCs by the ratio of the angular momentum to eccentricity L_z/e in the NFWBB axisymmetric model (left panel), the Allen & Santillan model (middle panel), and the Irrgang III model (right panel).

Table 2
Parameters of the Gaussian Components in Figure 2

Parameter	NFWBB Model		Allen & Santillan Model		Irrgang III Model	
	Gaussian Components:		Gaussian Components:		Gaussian Components:	
	Left-hand	Right-hand	Left-hand	Right-hand	Left-hand	Right-hand
Amplitude	20	6	23	6	18	7
Mean value (m), (kpc km s^{-1})	6	1470	−116	1304	13	1319
Standard deviation (σ), (kpc km s^{-1})	249	496	235	390	244	332

GC samples within corresponding error bars in the distances, the proper motions, and the line-of-sight velocities. The errors in proper motions and the line-of-sight velocities were taken from Vasiliev (2019). The distances for the artificial data sets were assigned assuming 5% and 10% uncertainties in the individual distances to the clusters. For each artificial data set we find the average radial $\langle\Pi\rangle$ and rotational $\langle\Theta\rangle$ velocities for the bar/bulge, the thick disk, and the halo. The velocities of the subsystems of GCs and the determined errors are listed in Table 3. Figure 3 shows the histograms of the GCs' velocity distributions in the bar/bulge, the thick disk, and the halo of the Milky Way. Figure 4 shows the distribution of the subsystem objects in the diagram "E–L_z." It is interesting to note the specific location of the bar/bulge and the thick-disk objects.

3.2.1. Bar/Bulge

Velocities of the subsystems of the GCs are given in Table 3. Figure 3 (top panels) shows the velocity distributions of the GCs belonging to the bar/bulge of the Milky Way. We find the average rotational velocity of the GCs within the bar/bulge of 49 ± 11 km s^{-1}. The Milky Way bulge kinematics has been a subject of extensive studies in recent years. Using the Bulge Radial Velocity Assay survey, Howard et al. (2008) find that the rotational velocity of bulge stars changes between −100 and +80 km s^{-1} within $-10^\circ \leqslant l \leqslant +10^\circ$. This estimate agrees with Kunder et al. (2012), who find that the rotational velocity of bulge stars changes from −100 to +80 km s^{-1} over the bulge region they surveyed. Ness et al. (2012) also find that for $-10^\circ \leqslant l \leqslant +10^\circ$ the bulge rotational velocity changes within −100 to +80 km s^{-1} (see their Figure 3). Finally, Zoccali et al. (2014, their Figure 6), using the GIRAFFE inner bulge survey, find that the rotational velocity of the sample of bulge red clump stars changes from ∼+75 to ∼−75 km s^{-1}. All these studies confine the rotation curve in Galactic longitude $-10^\circ \leqslant l \leqslant +10^\circ$, which translates into Cartesian Galactocentric coordinate Y in the range ±1.3 kpc. A close inspection of Table A1 shows that all the GCs marked as bulge clusters satisfy this constraint. With the poor statistics of our bulge GCs we cannot clearly derive the bulge rotation curve. Still, our estimate of the bulge average rotational velocity as traced by GCs is 49 ± 11 km s^{-1} and falls well within the reported determinations.

3.2.2. Thick Disk

Figure 3 (middle panels) shows the velocity distributions of the GCs belonging to the thick disk of the Milky Way. The main kinematical feature of the GCs within the thick Milky Way disk is their significant rotation. Our estimate of the rotational velocity of the GCs, belonging to the thick Milky Way disk, yields the value of 179 ± 6 km s^{-1} with the lag of the rotational velocity relative to the assumed velocity of LSR of 59–71 km s^{-1}. This value of the lag between the rotational velocity of the thick-disk GCs and the rotational velocity of LSR is roughly comparable to the lag of the thick-disk stars relative to the stellar Milky Way thin disk as estimated by Pasetto et al. (2012) to be about 49 ± 6 km s^{-1}.

3.2.3. Halo

Figure 3 (bottom panels) shows the velocity distributions of the GCs that belong to the halo of the Milky Way. As one can clearly see from the figure, the velocity distributions of the halo GCs can be approximated by Gaussian distributions both in the radial and in the azimuthal directions. The estimated values for the average velocities are $\langle\Pi\rangle = -14 \pm 4$ km s^{-1}, $\langle\Theta\rangle = 1 \pm 4$ km s^{-1}. The value of the rotation velocity is close to zero, and we can conclude that the halo as traced by GCs does not rotate on average.

3.3. Comparison with the Results of Massari et al. (2019)

We now compare our criterion based on the orbital parameter L_z/e with the criterion based on the orbital parameter

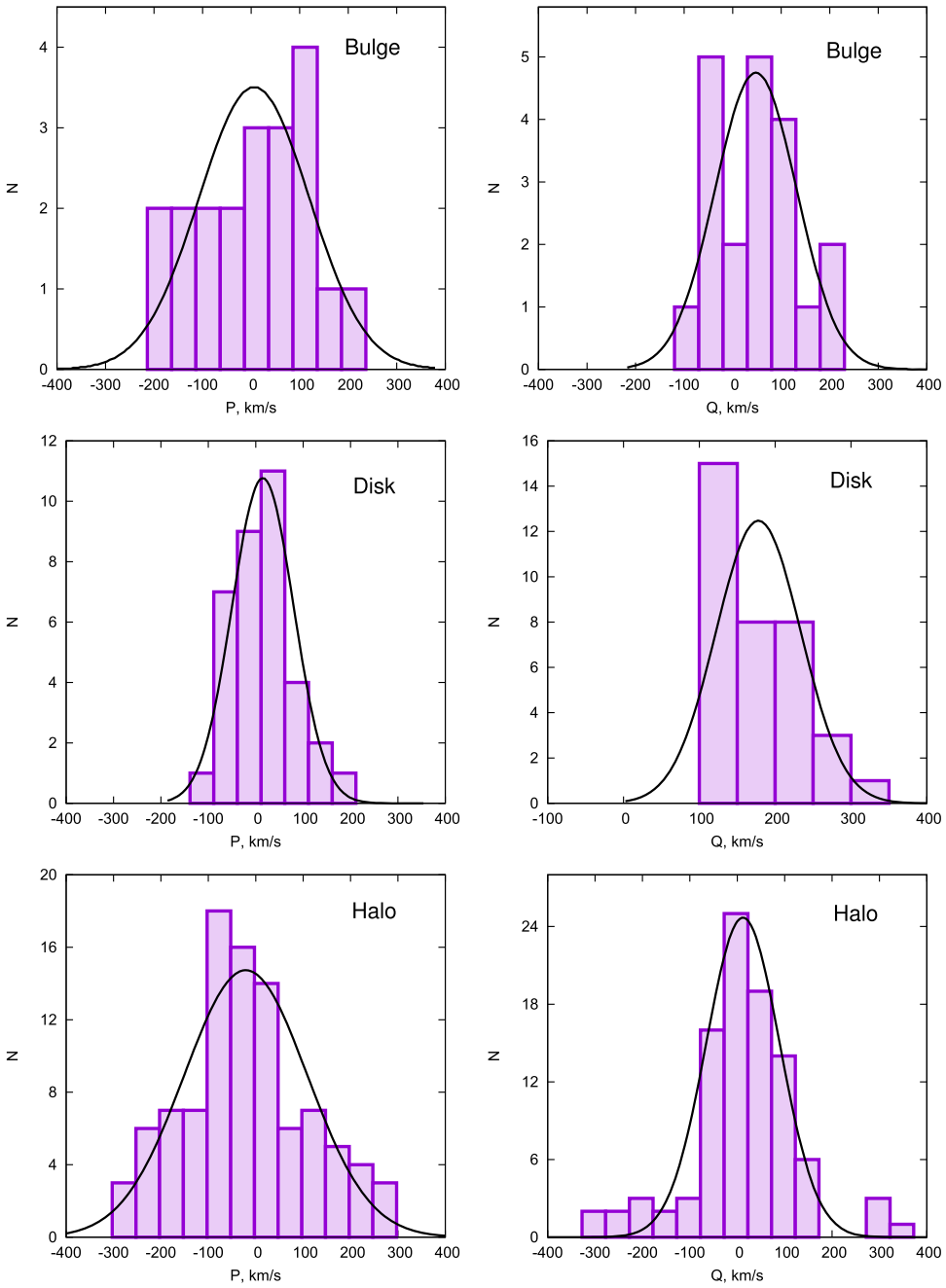

Figure 3. Histograms of $\langle\Pi\rangle$ and $\langle\Theta\rangle$ velocity distributions for GCs of the bar/bulge (top row), the thick disk (middle row), and the halo (bottom row).

Table 3
Average Velocities of the Subsystems of the GCs

Galaxy Subsystem (Number of GCs)	NFWBB Model (5%)		NFWBB Model (10%)		Allen & Santillán Model		Irrgang III Model	
	$\langle\Pi\rangle$ (km s^{-1})	$\langle\Theta\rangle$ (km s^{-1})	$\langle\Pi\rangle$ (km s^{-1})	$\langle\Theta\rangle$ (km s^{-1})	$\langle\Pi\rangle$ (km s^{-1})	$\langle\Theta\rangle$ (km s^{-1})	$\langle\Pi\rangle$ (km s^{-1})	$\langle\Theta\rangle$ (km s^{-1})
Bar/bulge (20)	4 ± 12	49 ± 11	4 ± 20	50 ± 15	3 ± 12	35 ± 10	4 ± 19	47 ± 13
Thick disk (35)	17 ± 5	179 ± 6	17 ± 7	179 ± 7	15 ± 6	165 ± 6	17 ± 6	177 ± 4
Halo (96)	-14 ± 4	1 ± 4	-15 ± 5	0 ± 6	-12 ± 5	-4 ± 4	-14 ± 5	0 ± 5

Circ (Massari et al. 2019) for separation of the GCs located in the thick-disk area ($Z < 5$ kpc) into the disk and halo clusters. We restrict ourselves to the procedure described in Section 3.1 of Massari et al. (2019) only, who use purely dynamical considerations to categorize star clusters. We stress in fact that our methodology is purely dynamical.

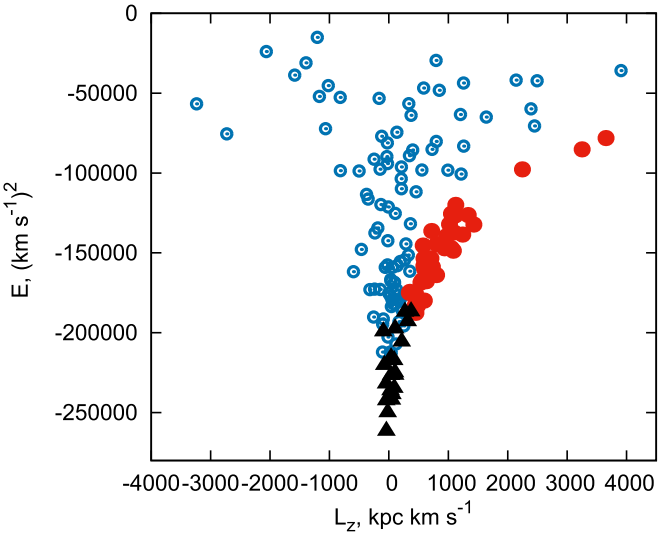

Figure 4. Distribution of the bar/bulge (black triangles), the thick disk (red closed circles), and the halo (blue open circles) GCs in the diagram "E–L_z."

We made a comparison under equal conditions using the NFWBB gravitational potential and the same conditions for the preliminary selection of the bulge/bar (apo <3.5 kpc) and halo ($Z_{\max} > 5$ kpc) objects. As a result, we get 36 bulge objects and 57 halo objects.

According to Massari et al. (2019), the separation of the remaining 58 GCs (in the band $|Z| < 5$ kpc) into the disk and halo is performed using the criterion Circ > 0.5. Such a condition is justified by the histogram shown in their Figure 5 (left panel). In this histogram the bimodality in the GCs' distribution is clearly visible. Using this very same criterion, we obtained 33 candidate disk members. The resulting list of objects differs from the list of objects obtained by Massari et al. (2019) by just five objects. These are NGC 6171, NGC 6333, NGC 6402, NGC 6441, and Djorg 1, with high eccentricities 0.72, 0.74, 0.88, 0.66, and 0.76, respectively, and look like impostors. Our criterion based on the bimodality of GCs' distribution on parameter L_z/e (see Figure 5, right panel) returns therefore 28 disk objects that coincide with the Massari et al. (2019) list. Thus, using our separation criterion based on the L_z/e parameter, we confirmed the result from Massari et al. (2019), which was obtained for another potential, while the use of the criterion based on the Circ orbit circularity parameter gave slightly different results.

4. Testing the GCs' Separation Criteria in the Axisymmetric Allen & Santillan and the Axisymmetric Irrgang III Potentials

The separation criterion was further checked against different realizations of the Galactic gravitational potential. To this purpose, we choose the most popular models of the Galactic potential: the model proposed by Allen & Santillan (1991), and the NFW model, modified by Irrgang et al. (2013) on the basis of data on Galactic masers. We denote these potentials as the Allen & Santillan and the Irrgang III models for the sake of brevity. The rotation curves corresponding to the NFWBB, Allen & Santillan, and Irrgang III potential models are shown in Figure 6, for comparison.

The Allen & Santillan model assumes that the Galactocentric distance of the Sun is $R_\odot = 8.5$ kpc and that the circular rotational velocity of the LSR is $V_\odot = 220\,\mathrm{km\,s^{-1}}$; therefore, the rotation curve differs considerably from the NFWBB model both at small ($R < 35$ kpc) and at large ($R > 35$ kpc) Galactocentric distances. On the other hand, the Irrgang III model and the NFWBB model are close to $R = 20$ kpc because they were constructed on the very same maser data. This can be seen clearly from the rotation curves in Figure 6. Both models have the same LSR velocity $V_\odot = 244\,\mathrm{km\,s^{-1}}$ and the same Galactocentric distance of the Sun $R_\odot = 8.3$. At larger distances, though, the rotation curve corresponding to the Irrgang III potential goes significantly higher than ours. Such a difference in the rotation curves is due to the fact that our potential was built using data up to 200 kpc, while the Irrgang III potential employs data up to 20 kpc only.

If we apply our separation algorithm to the disk layer ($|Z| < 6$ kpc), we obtain essentially the same result as employing our potential (see previous sections), despite the fact that slightly different L_z, e, and L_z/e are found. This happens because, especially in the case of the Irrgang III potential, distant objects are heavily influenced by rotation curves that deviate at large R. These distant objects are anyway cut off as halo objects already at the first stage of the separation algorithm. So they do not affect the separation of the GCs inside the disk layer ($|Z| < 6$ kpc). The disk objects are in fact situated within $R < 20$ kpc, and the Irrgang III potential affects their selection in the same way as in the case of our NFWBB potential owing to the proximity of the rotation curves for this Galactocentric distance range. In the case of the Allen & Santillan potential, the orbits of objects within $R < 20$ kpc undergo a more significant change than in the case of the Irrgang III potential. Nevertheless, the separation of objects in the disk layer $|Z| < 6$ kpc remains the same despite the change in the parameters L_z and e, simply because the distribution of L_z/e does not change.

The comparison of orbital parameters, namely, the eccentricity e, the Z projection of angular momentum L_z, and maximal values of coordinates $R_{\max}$, $Z_{\max}$, obtained in these three axisymmetric potentials is given in Figure 7. We stress the overall good correlation of the parameters for the majority of the GCs. In particular, good correlation of parameters $R_{\max}$, $Z_{\max}$ is maintained up to 20 kpc, where the majority of the GCs are concentrated. At larger distances, the mass of the halo plays an important role. But, as we already underlined above, distant objects are cut off as halo objects already at the first stage of the separation algorithm.

The second stage of separation, based on the bimodality of the L_z/e distribution, is shown in Figure 2, left panel for the NFWBB model, middle panel for the Allen & Santillan model, and right panel for the Irrgang III model. The parameters of the Gaussian components are given in Table 2. In spite of the differences in the distribution of the GCs in all three models seen in Figure 2, the comparison of the kinematical properties of the GCs in the Milky Way subsystems shows that within the errors there is no difference in the average velocities of the thick disk and of the halo in these three models (see Table 3). Kinematical properties of bar/bulge GCs are close for the NFWBB and the Irrgang III models and differ, however, considerably from the Allen & Santillan model. Disagreement is caused, most probably, by the difference of the disk rotational curves in its central regions in the rotation curves: the NFW models (NFWBB and Irrgang III) of the galactic potential show a prominent hump on the rotation curve, while the Allen & Santillan model simply does not show it. As one

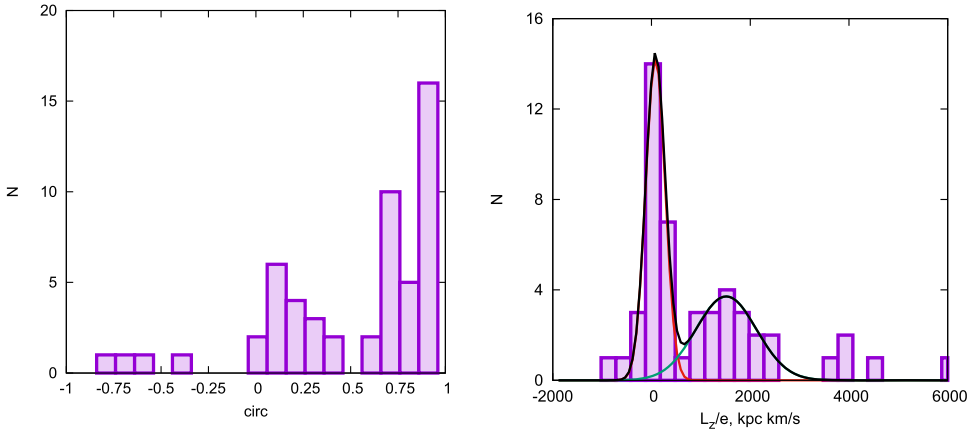

Figure 5. Distribution of the GCs by the parameter circ (left panel) and by the ratio of the angular momentum to the eccentricity L_z/e (right panel).

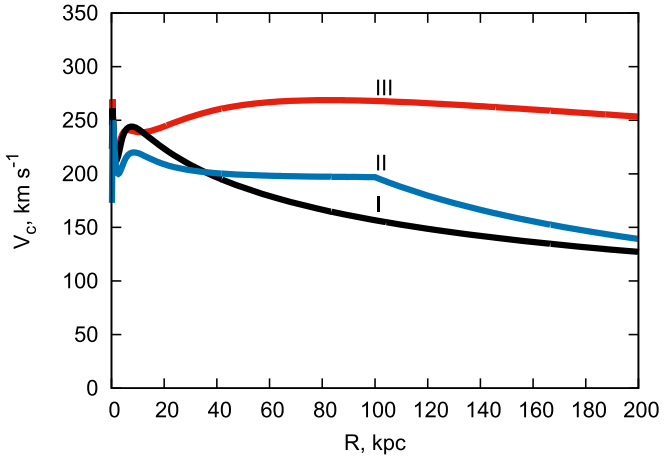

Figure 6. Rotation curves corresponding to the NFWBB (I), the Allen & Santillan (II), and the Irrgang (III) potential models.

can see from Table 3, within the errors different GC populations have the same kinematical properties in all three models of the Milky Way potential.

5. Testing GCs' Separation Criteria in Barred Potentials

In an attempt to better quantify the possible role of the bar/bulge potential, in this section we test the separation algorithm in case of the NFWBB potential complemented with the bar potential in the form of the triaxial ellipsoid model of Palouš et al. (1993) (see also Section 2). We adopted as the mass of the bar $M_{\rm bar} = 1.0 \times 10^{10} M_{\odot}$, wherein the bulge mass M_b is reduced by the mass of the bar. Since in the literature the rotational velocity of the Galactic bar is reported with large uncertainties, we checked our algorithm against four different values: $\Omega_{\rm bar} = 31$, 41, 55, and 70 kpc km s^{-1} (see Section 2).

Our splitting algorithm stands on the analysis of the L_z/e distribution. In the case of nonaxisymmetric potential the Z projection of angular momentum L_z is not constant along the orbit, and therefore we take the value $\langle L_z \rangle$ equal to the average value of L_z along the orbit. Orbits of the GCs, especially close to the Galactic center, can be noticeably affected by the bar. Particularly, eccentricities e of GCs' orbits can change significantly, thereby significantly changing the distribution $\langle L_z \rangle /e$. The orbital parameter e and the limits of variation of the L_z, as well as its mean value $\langle L_z \rangle$ for the GCs in the disk layer $|Z| < 6$ kpc obtained in the barred NFWBB potential for all adopted bar rotational velocities, are given in Table A2 of the Appendix. The comparison of the orbital parameters (e, L_z, L_z/e, $R_{\rm max}$, $Z_{\rm max}$) is given in Figure 8. The parameters obtained in the barred NFWBB potential with $\Omega_{\rm bar} = 31$ km s^{-1} kpc^{-1} and $\Omega_{\rm bar} = 55$ km s^{-1} kpc^{-1} are compared with the corresponding orbital parameters obtained in the axisymmetric NFWBB potential. We notice a general good correlation of the parameters for the majority of the GCs.

Nonetheless, as expected, the inclusion of a rotating bar affected the separation of the GCs close to the Galactic center. As a result, the number of bulge objects decreased from 20, as identified in the axisymmetric potential, to 16 for bar rotation velocities of 31, 41, and 55 km s^{-1} kpc^{-1} and to 15 for a bar velocity of 70 km s^{-1} kpc^{-1}. As a consequence, NGC 6355, Pismis 26, Djorg 2, and ESO 456-78 were dropped out of the list of the bar/bulge objects, and in the case of a bar velocity of 70 km s^{-1} kpc^{-1}, also NGC 6558. The selection of halo objects under the condition $Z_{\rm max} > 6$ kpc only changed slightly. The halo list was depleted by just the cluster E3, at bar velocities of 41, 55, and 70 km s^{-1} kpc^{-1}. The separation of the GCs into disk and halo objects inside the layer $|Z| < 6$ kpc has undergone the following changes depending on the bar velocity. At a bar velocity of 31 km s^{-1} kpc^{-1}, the number of disk objects became equal to 36 since NGC 6541 was dropped from the previous list while ESO 456-78 and NGC 6717 were added. At a bar velocity of 41 km s^{-1} kpc^{-1}, the number of disk objects became equal to 36 since E3 was dropped and ESO 456-78 and NGC 6717 were added. At a bar velocity of 55 km s^{-1} kpc^{-1}, the number of disk objects became equal to 37, since E3 dropped out of the previous list while ESO 456-78, Djorg 2, and NGC 6717 were added. Finally, at a bar velocity of 70 km s^{-1} kpc^{-1}, the number of disk objects became equal to 35 since E3 and NGC 6541 were dropped from the previous list while ESO 456-78 and NGC 6717 were added. Thus, from 35 disk objects identified in the axisymmetric potential, 33 objects are stably preserved. The largest influence of the bar turned out to be on GCs E3 and NGC 6541. Overall, we found little dependence of the results of the separation of GCs on the bar rotation velocity. The histograms of the GCs' distributions by the $\langle L_z \rangle /e$ parameter and the approximating Gaussian distributions for all the bar velocities are shown in Figure 9.

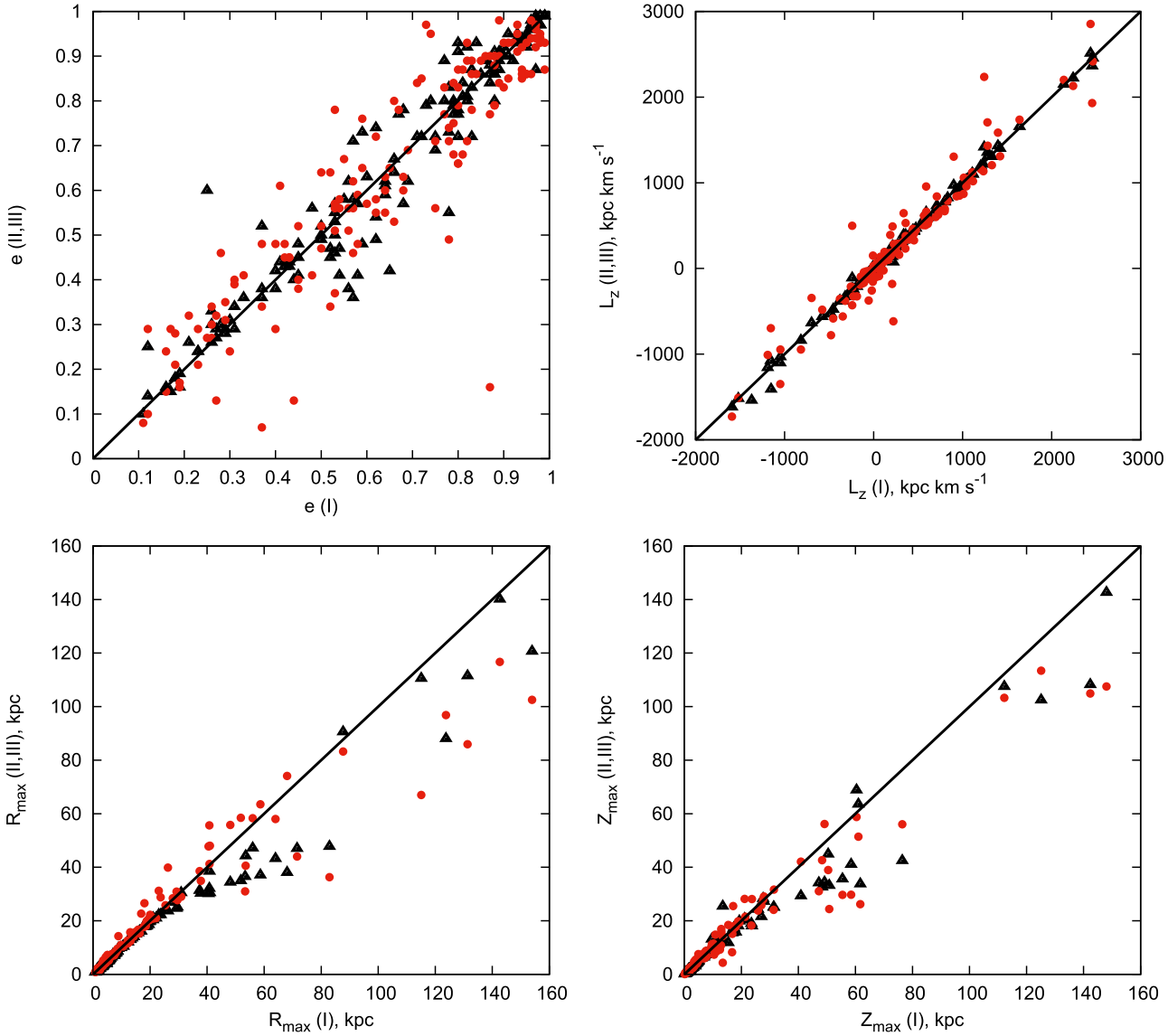

Figure 7. Comparison of the orbital parameters (e, L_z, R_{max}, Z_{max}) obtained in different axisymmetric potentials. The parameters obtained in the Allen & Santillan (red circles) and the Irrgang III (black triangles) potentials are compared with corresponding orbit parameters obtained in the NFWBB potential. In each panel we plot the line of coincidence.

6. Metallicities of the Cluster Subsystems

It has been known for a long time that GCs with low metal abundances are distributed throughout the volume of the halo and have a low concentration toward the Galactic plane, while clusters with high metal abundances are concentrated toward the Galactic plane and are found predominantly at distances inside the solar radius. Zinn (1993) showed that clusters with metallicities [Fe/H] $\leqslant -0.8$ dex belong to the Milky Way halo and have comparatively low rotational speeds and velocity dispersions while clusters with higher metal abundances belong to the disk subsystem.

Precise kinematical data of the Milky Way GCs allow us to address the problem of the chemical abundances of the GCs in a new way: to solve the general problem of the interrelation of the chemical abundances and the kinematical properties of the clusters. By assuming the separation of the clusters among the subsystems of the Galaxy, one can estimate the mean metallicities of the clusters that belong to the different subsystems of the Milky Way.

In order to take the chemical compositions of GCs in different Galactic subsystems into account, we used cluster metallicities taken from Harris (2010) and for the Crater cluster from Laevens et al. (2014). The left panel of Figure 10 shows the metallicity distribution for the halo and for the thick-disk cluster subsystems as a function of distance from the Galactic center. The open and filled symbols correspond to the halo and disk clusters, respectively. Together with clusters with high metal abundances and disk kinematics, several low-metallicity clusters also display kinematics typical of the disk subsystem. This result can also be seen in the middle panel of Figure 10, which presents the metallicity distributions of halo and thick-disk GCs as a function of the distance from the plane of the disk, Z. This figure shows that, together with clusters in the disk subsystem, GCs displaying halo kinematics (open symbols) are also concentrated toward the plane of the disk, probably reflecting some incompleteness of the sample.

The right panel of Figure 10 shows metallicity distributions as a function of Galactocentric radial velocities of halo GCs

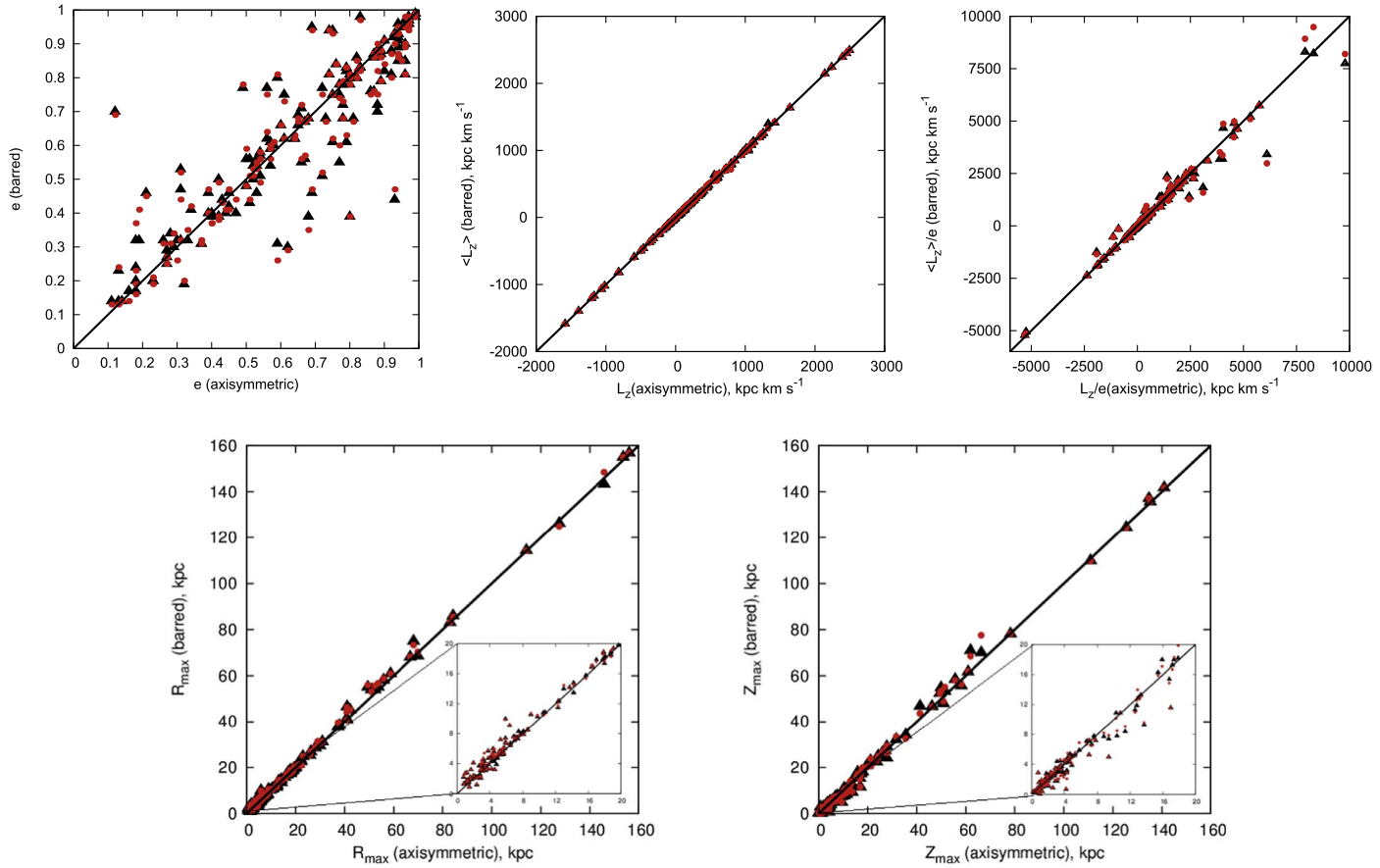

Figure 8. Comparison of the orbit parameters (e, $\langle L_z\rangle$, $\langle L_z\rangle/e$, $R_{\max}$, $Z_{\max}$). The parameters obtained in the barred NFWBB potential with $\Omega_{\rm bar} = 55$ km s^{-1} kpc^{-1} (red circles) and $\Omega_{\rm bar} = 31$ km s^{-1} kpc^{-1} (black triangles) are compared with corresponding orbit parameters obtained in the axisymmetric NFWBB potential. In each panel we plot the line of coincidence.

(open symbols) and disk GCs (filled symbols). This figure shows that a large fraction of disk GCs are located in the region with [Fe/H] $\geqslant -1.0$ dex, while most halo clusters have low metal abundances [Fe/H] $\leqslant -1.0$ dex. Virtually all clusters displaying halo kinematics have low metal abundances, and these clusters occupy a large range of radial velocities, right up to 300 km s^{-1}. We find that the mean metallicity for the disk GCs subsystem is equal to [Fe/H] $= -0.96 \pm 0.11$ dex, while for the halo objects the mean metallicity is equal to [Fe/H] $= -1.58 \pm 0.05$ dex, and for the GCs in the region of the bar/bulge the mean metallicity is equal to [Fe/H] $= -0.95 \pm 0.08$ dex. After the study of Forbes & Bridges (2010), retrograde motion has usually been considered to indicate that a GC was accreted during the evolution of the Galaxy. If this view is correct, we should expect differences in the mean metallicities for accreted halo GCs exhibiting retrograde motion and clusters orbiting in the Galactic prograde direction, which are presumed to have formed in situ during the evolution of the Galaxy. Cluster kinematics can be used to distinguish halo clusters in retrograde orbits and clusters rotating in the prograde direction. To elucidate the likelihood of possible differences in the chemical compositions of these groups of GCs, we applied a statistical Student's t-test. The mean metallicities of these two groups of clusters are statistically indistinguishable, which does not support the suggestion that these two groups of clusters have different origins.

On the other hand, the application of this test to the samples of GCs belonging to the disk and halo subsystems shows statistically significant differences, indicating that these two groups of clusters have different chemical evolution histories and probably different origin. The mean metallicity of bar/bulge GCs is statistically indistinguishable from the mean metallicity of the disk GC.

7. Summary

In this paper we presented a large suite of orbital integrations of the Milky Way GCs with the aim of determining their membership to different Galactic components. We summarize our main results as follows:

(i) We have used high-quality proper-motion data for nearly all known Milky Way GCs, together with known distances and the line-of-sight velocities, to study their kinematical properties of the Milky Way components. To assign clusters to the various subsystems of the Milky Way, we used their orbital parameter (ratio L_z/e) distribution, which was never applied before to the GC system of the Milky Way. We have shown that our splitting algorithm is stable against different realizations of the Galactic potential, in both the axisymmetric and nonaxisymmetric cases.

(ii) The orbits of the clusters and their orbital parameters clearly distinguish three groups of the clusters: those that belong to the bar/bulge of the Milky Way, the clusters

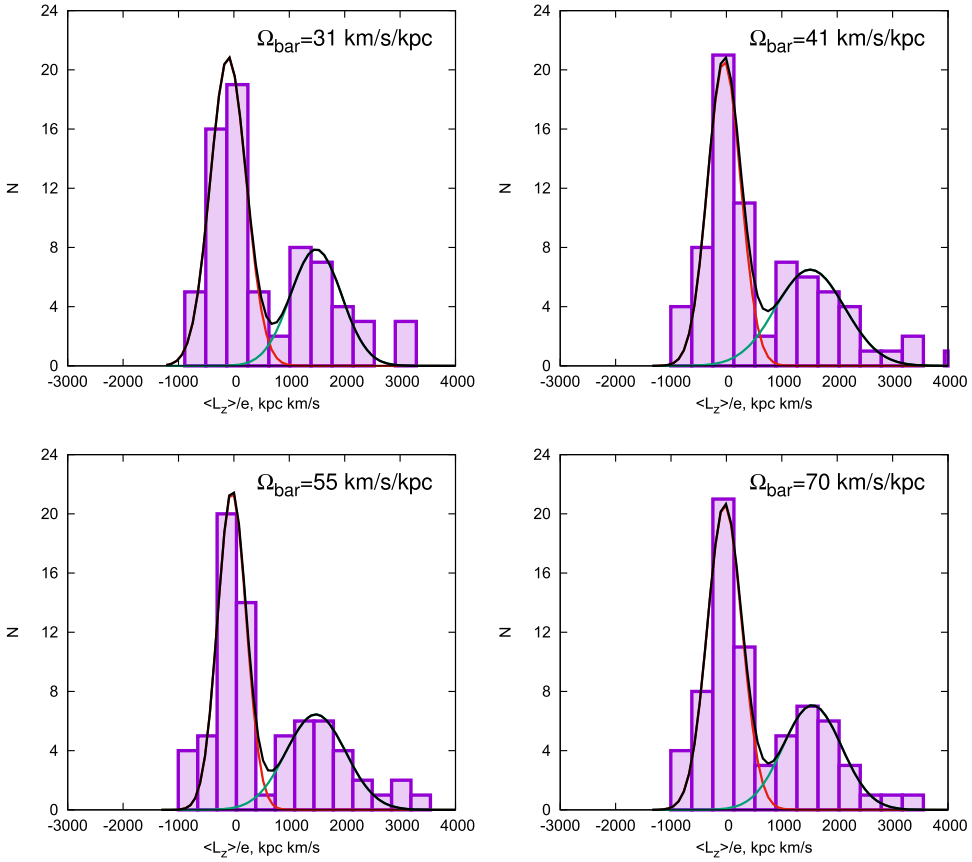

Figure 9. Distribution of the GCs by the ratio of the average angular momentum to eccentricity $\langle L_z \rangle / e$ for different bar velocities: $\Omega_{\rm bar} = 31$, 41, 55, and 70 km s^{-1} kpc^{-1}.

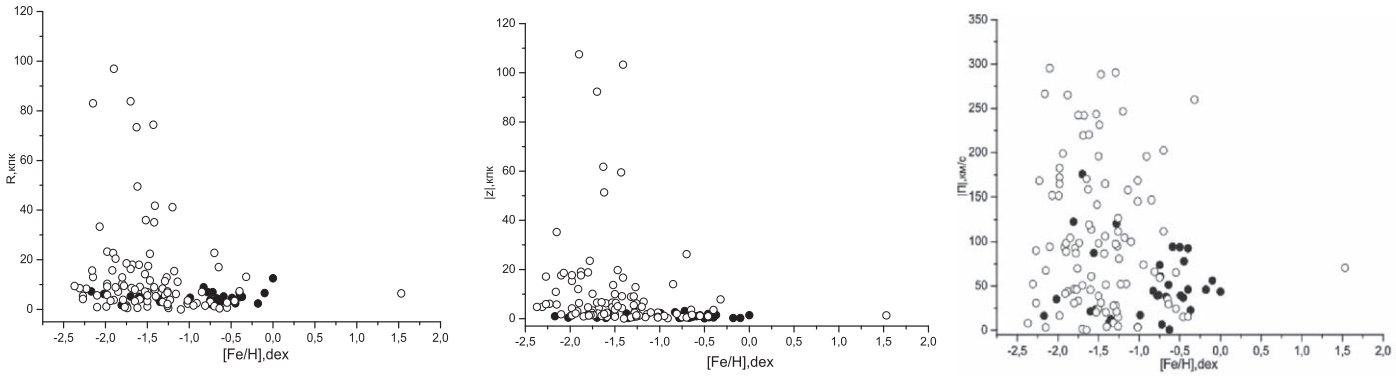

Figure 10. Distribution of the metallicities of GCs in the halo and thick-disk subsystems as a function of distance from the Galactic center (left panel), dependence of the metallicities of the GCs on distance from the Galactic plane Z (middle panel), and dependence of the metallicities of the GCs on the radial velocities of halo and disk (right panel). In all pictures the halo and disk clusters are marked by open and filled symbols, respectively.

that belong to the thick Milky Way disk, and the clusters belonging to the Milky Way halo.

(iii) The bar/bulge subsystem of the GCs has a relatively slow rotation of 49 ± 11 km s^{-1} and close to zero radial velocity for the ensemble of the GCs within the bar/bulge region.

(iv) The clusters distinguished by their kinematical properties as the members of the thick disk have rotational velocity of 179 ± 6 km s^{-1} consistent with the recent estimate of the rotational velocity of metal-weak stellar thick-disk population 182 ± 6 km s^{-1} (Tian et al. 2019).

The estimated lag in the rotational velocity of the GCs' thick disk and the rotational velocity of LSR is 65 ± 6 km s^{-1}, roughly consistent with the estimate of the lag of the rotational velocity between the stellar thick and thin disks found by Pasetto et al. (2012).

Our estimate of the rotational velocity of the thick-disk GCs differs from the recent estimate of the disk GCs' rotational velocity obtained by Posti & Helmi (2019), equal to 220 km s^{-1}, but is consistent with the recent estimate of the rotational velocity of the metal-weak thick-disk stellar population (Tian et al. 2019).

(v) We confirm previous findings that the subsystem of the GCs belonging to the Milky Way halo practically has rotation close to zero, 1 ± 4 km s^{-1}. We find, contrary to the conclusion of Posti & Helmi (2019), that the halo

GCs have a prograde rotation, and its rotational velocity is consistent with the estimated rotational velocity of the local stellar halo of 27^{+4}_{-5} km s^{-1} (Tian et al. 2019).

(vi) We have determined the mean metallicities for GCs with well-defined kinematic parameters and orbits in different subsystems of the Milky Way. The mean metallicity of GCs of the disk subsystem was found to be [Fe/H] $= -0.96 \pm 0.11$ dex and of the halo subsystem to be [Fe/H] $= -1.58 \pm 0.05$ dex. The mean metallicity of GCs associated with the bar/bulge was found to be [Fe/H] $= -0.95 \pm 0.08$ dex.

V.K. acknowledges financial support by Southern Federal University, 2020 (Ministry of Science and Higher Education of the Russian Federation). We acknowledge the anonymous referee for the valuable comments and suggestions.

Appendix

The parameters of all 151 GCs calculated in the NFWBB axisymmetric potential are given in Table A1. The parameters of GCs calculated in the barred NFWBB potential are given in Table A2.

Table A1
Orbit Parameters of GCs Obtained in the NFWBB Axisymmetric Potential

Name	X (kpc)	Y (kpc)	Z (kpc)	Π (km s^{-1})	Θ (km s^{-1})	W (km s^{-1})	e	Z_{max} (kpc)	R_{max} (kpc)	r_{max} (kpc)	L_z (kpc km s^{-1})	E (km s^{-1})^2	GS
NGC 104	6.4	−2.6	−3.2	6	192	45	0.16	3.4	7.5	7.7	1328	−126288	D
NGC 288	8.4	0.1	−8.9	9	−42	51	0.80	10.3	12.3	12.3	−349	−116280	H
NGC 362	5.2	−5.1	−6.2	127	−1	−70	0.98	10.4	12.3	12.3	−10	−121290	H
Whiting 1	22.3	4.7	−26.2	−208	109	8	0.53	60.9	66.8	67.0	2494	−42265	H
NGC 1261	8.2	−10.0	−12.8	−95	−19	69	0.94	16.8	21.1	21.1	−249	−91385	H
Pal 1	15.1	8.0	3.6	42	214	−20	0.13	4.5	19.1	19.1	3646	−78086	D
E 1	24.8	−80.1	−92.3	11	−144	96	0.31	135.2	231.9	237.9	−12100	−15914	H
Eridanus	61.5	−41.8	−59.5	−90	−28	133	0.87	140.9	145.9	174.5	−2064	−23988	H
Pal 2	34.8	4.4	−4.3	−108	11	4	0.97	13.7	40.9	41.0	373	−63896	H
NGC 1851	12.6	−8.9	−6.9	105	−1	−82	0.99	17.0	20.1	20.1	−22	−94063	H
NGC 1904	15.9	−8.3	−6.3	46	12	4	0.97	8.8	19.7	19.7	211	−96192	H
NGC 2298	12.6	−9.5	−3.0	−92	−32	77	0.87	11.4	18.0	18.0	−500	−98716	H
NGC 2419	83.0	−0.5	35.2	−5	47	−58	0.68	58.1	83.1	91.8	3907	−35896	H
Pyxis	14.2	−38.7	4.8	−247	−29	187	0.77	283.5	175.6	324.2	−1205	−15098	H
NGC 2808	6.3	−9.2	−1.9	−157	41	28	0.87	4.9	14.2	14.4	457	−111797	H
E 3	5.4	−7.1	−2.6	44	251	104	0.18	5.8	13.0	13.1	2240	−97684	D
Pal 3	42.6	−59.7	61.8	−147	89	67	0.39	134.7	153.7	173.4	6495	−20091	H
NGC 3201	7.7	−4.8	0.8	−114	−301	151	0.52	10.8	26.2	26.3	−2728	−75483	H
Pal 4	39.7	−12.9	103.3	−25	−33	56	0.75	110.9	114.1	116.5	−1394	−31065	H
Crater	0.2	−97.0	107.5	−101	−63	63	0.14	125.4	156.1	156.1	−6104	−18859	H
NGC 4147	9.6	−4.1	18.8	47	−3	128	0.97	26.0	25.8	26.4	−27	−81117	H
NGC 4372	5.4	−4.9	−1.0	16	133	67	0.42	2.1	7.3	7.3	962	−139570	D
Rup 106	−2.4	−17.8	4.3	−242	91	32	0.78	23.7	37.9	37.9	1640	−64986	H
NGC 4590	4.2	−7.2	6.1	−169	293	16	0.54	17.9	29.0	29.9	2453	−70495	H
NGC 4833	4.7	−5.4	−0.9	105	40	−42	0.83	3.5	8.0	8.0	286	−144428	H
NGC 5024	5.5	−1.5	17.6	−95	141	−72	0.43	21.4	22.1	22.3	797	−80241	H
NGC 5053	5.3	−1.4	17.1	−89	134	35	0.27	17.4	17.8	18.0	727	−85221	H
NGC 5139	5.1	−3.9	1.4	−70	−72	−80	0.73	2.8	7.4	7.4	−462	−147850	H
NGC 5272	6.8	1.3	10.0	−38	143	−134	0.51	13.3	15.7	15.9	994	−98226	H
NGC 5286	0.7	−8.6	2.2	−220	−44	10	0.89	7.0	13.7	13.7	−375	−113332	H
NGC 5466	5.0	3.0	15.4	172	−141	226	0.80	49.4	53.6	53.7	−820	−52693	H
NGC 5634	−7.4	−5.0	19.1	−45	39	−26	0.82	19.7	21.1	21.6	346	−89143	H
NGC 5694	−18.1	−14.6	17.7	−185	−44	−166	0.93	46.2	69.9	70.4	−1019	−45290	H
IC 4499	−2.4	−14.0	−6.6	−245	−75	−62	0.65	27.1	29.8	30.0	−1066	−72235	H
NGC 5824	−18.1	−13.7	12.1	−41	105	−183	0.45	31.6	37.3	37.4	2393	−59779	H
Pal 5	−7.9	0.2	16.7	−54	160	−10	0.27	17.2	18.8	18.9	1260	−83194	H
NGC 5897	−2.0	−3.2	6.3	88	97	90	0.64	7.6	8.6	8.7	362	−131771	H
NGC 5904	3.2	0.4	5.5	−290	126	−181	0.82	21.1	23.0	23.3	402	−85576	H
NGC 5927	1.9	−4.2	0.7	−39	233	5	0.11	0.7	5.2	5.2	1077	−148662	D
NGC 5946	−0.6	−5.7	0.8	35	25	108	0.89	4.3	5.8	5.9	141	−158006	H
ESO 224-8	−7.8	−9.9	1.5	−43	259	0	0.18	1.9	17.0	17.0	3245	−85205	D
NGC 5986	−1.0	−4.0	2.4	62	23	−14	0.92	3.8	4.9	5.0	94	−168505	H
FSR 1716	0.1	−4.8	−0.3	87	228	−139	0.28	2.5	6.9	7.0	1089	−137191	D
Pal 14	−41.4	27.3	51.4	117	16	131	0.97	66.4	127.5	133.9	794	−29458	H
BH 184	1.5	−4.1	−0.4	40	121	−89	0.47	1.5	4.6	4.7	531	−168579	D
NGC 6093	−1.1	−1.2	3.4	33	16	−61	0.97	3.7	4.6	4.6	25	−176933	H
NGC 6121	6.2	−0.3	0.6	−52	10	−9	0.97	4.2	6.5	6.5	60	−159021	H
NGC 6101	−2.7	−10.0	−4.2	−12	−314	−195	0.61	24.3	42.2	44.2	−3236	−56722	H

Table A1
(Continued)

Name	X (kpc)	Y (kpc)	Z (kpc)	Π (km s^{-1})	Θ (km s^{-1})	W (km s^{-1})	e	Z_{max} (kpc)	R_{max} (kpc)	r_{max} (kpc)	L_z (kpc km s^{-1})	E (km s^{-1})^2	GS
NGC 6144	−0.2	−1.2	2.4	−69	−196	43	0.21	2.9	2.9	3.3	−239	−172662	H
NGC 6139	−1.3	−3.0	1.2	−1	76	137	0.54	2.7	3.4	3.6	248	−176480	H
Terzan 3	0.5	−2.1	1.3	−61	206	99	0.18	1.9	3.0	3.2	440	−175324	D
NGC 6171	2.4	0.4	2.5	−4	78	−65	0.72	2.8	3.7	3.8	191	−178959	H
ESO 452-11	0.3	−1.1	1.8	−24	−13	−104	0.98	2.2	2.9	2.9	−16	−202684	H
NGC 6205	5.5	4.6	4.7	20	−26	−80	0.79	7.8	8.6	8.6	−187	−134416	H
NGC 6229	1.8	22.3	19.8	30	6	51	0.97	27.8	30.9	31.0	135	−74434	H
NGC 6218	4.2	1.2	2.1	−9	135	−82	0.37	2.7	4.9	5.0	581	−158135	D
FSR 1735	−1.8	−3.8	−0.3	−102	−5	201	0.69	5.3	5.2	5.3	−22	−157538	H
NGC 6235	−2.9	−0.2	2.7	159	197	−40	0.39	4.5	5.9	6.2	570	−145439	D
NGC 6254	4.4	1.1	1.7	−87	134	48	0.42	2.4	5.2	5.2	606	−157472	D
NGC 6256	−1.8	−2.2	0.6	−170	28	97	0.92	3.1	4.2	4.2	79	−181873	H
Pal 15	−30.6	13.3	18.6	154	−5	50	0.96	50.8	49.4	54.6	−165	−53233	H
NGC 6266	1.6	−0.8	0.9	42	122	69	0.62	1.0	2.5	2.5	215	−205537	B
NGC 6273	−0.4	−0.5	1.5	−98	−240	179	0.59	3.5	3.8	3.9	−144	−172941	H
NGC 6284	−6.8	−0.4	2.7	14	−2	112	0.83	7.3	7.0	7.5	−16	−142332	H
NGC 6287	−0.9	0.0	1.8	−301	−64	79	0.75	5.2	5.3	5.3	−60	−159009	H
NGC 6293	−1.1	−0.4	1.3	−152	−80	−158	0.91	2.5	3.6	3.6	−93	−191358	H
NGC 6304	2.4	−0.4	0.6	79	191	72	0.29	1.0	3.2	3.3	474	−183132	D
NGC 6316	−2.0	−0.5	1.1	103	51	86	0.77	1.5	2.9	3.0	106	−197316	B
NGC 6341	5.8	6.3	4.8	53	13	95	0.94	9.4	10.7	10.7	108	−125312	H
NGC 6325	0.6	0.1	1.1	−81	−181	79	0.12	1.2	1.2	1.4	−107	−212097	H
NGC 6333	0.6	0.8	1.5	−89	346	68	0.74	4.1	6.4	6.4	327	−151409	H
NGC 6342	−0.1	0.7	1.5	−25	164	−32	0.31	1.5	1.6	1.7	117	−207010	H
NGC 6356	−6.5	1.7	2.7	47	107	110	0.52	4.5	7.8	7.9	713	−136303	D
NGC 6355	−0.9	−0.1	0.9	−207	−110	144	0.56	1.9	2.0	2.2	−95	−199192	B
NGC 6352	3.0	−1.8	−0.7	42	226	7	0.13	0.7	4.1	4.1	794	−163864	D
IC 1257	−14.8	6.9	6.5	−45	−50	−20	0.82	6.7	18.1	18.1	−817	−98556	H
Terzan 2	0.8	−0.5	0.3	−120	−47	−44	0.86	0.7	1.2	1.2	−44	−242360	B
NGC 6366	5.1	1.1	1.0	94	134	−62	0.45	2.0	5.8	5.8	699	−153378	D
Terzan 4	1.1	−0.5	0.2	15	75	97	0.68	0.8	1.3	1.3	92	−234494	B
BH 229	0.1	−0.4	0.3	7	−55	−287	0.49	0.8	0.8	0.8	−21	−249808	B
NGC 6362	2.3	−4.1	−2.3	17	124	100	0.37	3.3	5.2	5.3	583	−153468	D
Liller 1	0.1	−0.7	−0.0	107	−56	25	0.81	0.2	0.8	0.8	−42	−261395	B
NGC 6380	−2.4	−1.9	−0.6	−62	−35	14	0.89	2.1	3.4	3.4	−105	−194646	H
Terzan 1	1.6	−0.3	0.1	−73	63	5	0.79	1.0	1.8	1.8	102	−224803	B
Pismis 26	0.2	−1.3	−0.5	−112	204	200	0.56	1.8	3.2	3.2	271	−186876	B
NGC 6388	−1.2	−2.5	−1.1	−66	−94	−16	0.69	1.6	3.5	3.5	−257	−190150	H
NGC 6402	−0.1	3.3	2.4	−20	48	23	0.88	2.8	4.8	4.8	158	−176457	H
NGC 6401	−2.3	0.6	0.8	−30	−254	161	0.31	2.3	4.4	4.5	−595	−161761	H
NGC 6397	6.2	−0.8	−0.5	35	127	−121	0.40	2.9	6.5	6.5	796	−144538	D
Pal 6	2.5	0.2	0.2	−191	21	153	0.95	3.3	4.5	4.5	52	−179351	H
NGC 6426	−9.2	9.3	5.8	−112	93	−26	0.67	7.0	16.5	16.6	1216	−100666	H
Djorg 1	−1.0	−0.5	−0.4	−252	315	28	0.76	2.6	5.9	6.0	351	−161437	H
Terzan 5	1.4	0.5	0.2	84	70	−31	0.77	0.8	1.7	1.7	104	−226313	B
NGC 6440	−0.1	1.1	0.6	91	−42	−39	0.78	1.1	1.4	1.4	−49	−231796	B
NGC 6441	−3.2	−1.3	−1.0	16	66	−21	0.66	1.4	3.5	3.6	228	−186312	H
Terzan 6	1.5	−0.2	−0.2	−138	−51	42	0.86	1.3	2.0	2.0	−77	−220185	B
NGC 6453	−3.2	−0.9	−0.8	−105	38	−159	0.61	3.6	3.8	3.9	129	−172906	H
NGC 6496	−2.6	−2.3	−2.0	−37	320	−60	0.42	4.0	9.0	9.1	1111	−126509	D
Terzan 9	1.2	0.5	−0.2	−50	22	−53	0.92	1.0	1.4	1.4	29	−236057	B
Djorg 2	2.0	0.3	−0.3	161	155	−45	0.57	0.4	3.2	3.2	316	−192751	B
NGC 6517	−1.6	3.5	1.3	55	33	−34	0.90	2.9	4.5	4.5	127	−179281	H
Terzan 10	−2.1	0.8	−0.3	231	87	239	0.79	4.7	5.9	5.9	193	−155422	H
NGC 6522	0.6	0.1	−0.5	34	92	−189	0.67	0.9	1.2	1.2	58	−238519	B
NGC 6535	2.4	3.0	1.3	93	−83	45	0.64	1.6	4.5	4.6	−320	−173024	H
NGC 6528	0.4	0.2	−0.6	−197	113	−32	0.60	0.9	1.0	1.0	51	−241883	B
NGC 6539	1.1	2.8	0.9	1	118	172	0.30	2.5	3.2	3.4	347	−174387	D
NGC 6540	3.0	0.3	−0.3	13	148	57	0.32	0.5	3.0	3.1	448	−187517	D
NGC 6544	5.3	0.3	−0.1	6	6	−90	0.98	4.3	5.7	5.7	31	−166630	H
NGC 6541	1.1	−1.4	−1.4	123	192	−112	0.50	2.4	3.8	3.8	334	−174968	D
ESO 280-06	−12.0	−4.7	−4.6	31	16	−84	0.88	12.6	14.2	14.2	210	−109791	H
NGC 6553	2.3	0.6	−0.3	45	245	−5	0.19	0.3	3.3	3.3	588	−179839	D

Table A1
(Continued)

Name	X (kpc)	Y (kpc)	Z (kpc)	Π (km s^{-1})	Θ (km s^{-1})	W (km s^{-1})	e	Z_{max} (kpc)	R_{max} (kpc)	r_{max} (kpc)	L_z (kpc km s^{-1})	E (km s^{-1})^2	GS
NGC 6558	0.9	0.0	−0.8	187	93	15	0.72	1.4	1.7	1.7	87	−217130	B
Pal 7	3.3	2.0	0.6	−74	270	27	0.26	0.8	6.0	6.0	1042	−147032	D
Terzan 12	3.5	0.7	−0.2	−94	172	97	0.33	1.3	4.3	4.4	625	−167749	D
NGC 6569	−2.5	0.1	−1.3	−40	174	25	0.23	1.3	2.9	3.0	440	−182361	D
ESO 456-78	1.8	0.4	−0.6	71	199	−139	0.34	1.3	2.9	2.9	373	−186632	B
NGC 6584	−4.0	−4.0	−3.8	197	98	−238	0.83	12.9	17.9	18.0	556	−98089	H
NGC 6624	0.5	0.4	−1.1	−29	60	−119	0.78	1.3	1.5	1.5	37	−226410	B
NGC 6626	2.9	0.7	−0.5	−28	57	−93	0.75	1.9	3.1	3.1	169	−193067	H
NGC 6638	−0.9	1.3	−1.1	68	14	26	0.96	1.8	2.4	2.4	22	−212068	H
NGC 6637	−0.4	0.3	−1.6	35	91	85	0.94	1.7	2.4	2.4	40	−212500	H
NGC 6642	0.4	1.4	−0.9	112	25	−50	0.94	1.6	2.2	2.2	36	−215457	B
NGC 6652	−1.5	0.3	−2.0	−54	28	176	0.96	3.1	4.2	4.2	42	−183595	H
NGC 6656	5.2	0.6	−0.4	176	201	−143	0.53	3.5	9.8	9.8	1044	−125471	D
Pal 8	−4.0	3.1	−1.5	−21	117	−29	0.51	1.7	5.5	5.6	593	−160020	D
NGC 6681	−0.5	0.4	−1.9	221	55	−176	0.74	4.4	4.5	4.5	36	−167768	H
NGC 6712	2.1	3.0	−0.5	146	26	−146	0.94	3.9	5.5	5.5	93	−168544	H
NGC 6715	−17.3	2.5	−6.4	232	49	210	0.58	51.4	52.3	56.4	850	−48159	H
NGC 6717	1.5	1.6	−1.3	−10	116	25	0.59	1.4	2.8	2.8	251	−195762	H
NGC 6723	−0.0	0.0	−2.6	100	−178	−38	0.26	3.1	2.7	3.1	−2	−175356	H
NGC 6749	1.9	4.7	−0.3	−23	110	2	0.53	0.3	5.1	5.1	556	−167068	D
NGC 6752	5.0	−1.4	−1.7	−23	179	59	0.23	2.0	5.6	5.7	931	−147164	D
NGC 6760	2.3	4.3	−0.5	92	147	−15	0.44	0.5	5.5	5.6	724	−158732	D
NGC 6779	4.0	8.3	1.4	155	−15	99	0.96	9.4	12.4	12.4	−135	−119696	H
Terzan 7	−13.1	1.3	−7.8	260	25	185	0.54	41.3	41.0	42.9	335	−56545	H
Pal 10	4.7	4.7	0.3	−56	186	21	0.27	0.4	7.0	7.0	1234	−138495	D
Arp 2	−18.1	4.0	−10.1	243	68	181	0.57	55.6	58.7	65.1	1256	−43628	H
NGC 6809	3.4	0.8	−2.1	−199	76	−55	0.66	4.7	5.7	5.7	266	−154417	H
Terzan 8	−15.5	2.4	−10.9	269	37	161	0.57	49.9	50.9	58.5	584	−46785	H
Pal 11	−2.7	6.8	−3.6	−16	139	−7	0.40	3.6	8.1	8.2	1013	−132057	D
NGC 6838	6.1	3.3	−0.3	39	204	39	0.18	0.7	7.3	7.3	1423	−132307	D
NGC 6864	−9.4	6.5	−9.1	−99	18	48	0.94	12.8	16.4	16.4	209	−103615	H
NGC 6934	−0.8	11.7	−5.0	−289	103	122	0.88	15.4	40.8	40.9	1204	−63341	H
NGC 6981	−3.4	8.2	−9.2	−154	−4	170	0.97	15.9	22.3	22.3	−35	−89723	H
NGC 7006	−8.9	34.9	−13.7	−140	−33	86	0.90	35.5	55.8	56.3	−1170	−52073	H
NGC 7078	4.4	8.4	−4.8	8	118	−27	0.50	4.9	10.5	10.6	1119	−119947	D
NGC 7089	2.7	7.5	−6.7	170	−18	−173	0.94	13.0	18.8	18.8	−147	−97640	H
NGC 7099	3.4	2.5	−5.9	−32	−55	109	0.78	7.0	8.1	8.2	−234	−137480	H
Pal 12	−2.7	6.5	−14.0	146	304	115	0.65	61.9	68.2	72.0	2142	−41826	H
Pal 13	7.3	19.1	−17.6	268	−78	−78	0.83	78.3	84.3	87.1	−1586	−38661	H
NGC 7492	1.3	9.4	−23.5	−87	−13	64	0.80	27.8	28.0	28.1	−120	−77041	H

Table A2
Orbit Parameters of GCs in Barred NFWBB Potential

Name	$\Omega_{\rm bar} = 31$ km s^{-1} kpc^{-1}			$\Omega_{\rm bar} = 41$ km s^{-1} kpc^{-1}			$\Omega_{\rm bar} = 55$ km s^{-1} kpc^{-1}			$\Omega_{\rm bar} = 70$ km s^{-1} kpc^{-1}		
	e	$[L_z^{\max}, L_z^{\min}]$ (kpc km s^{-1})	$\langle L_z \rangle$ (kpc km s^{-1})	e	$[L_z^{\max}, L_z^{\min}]$ (kpc km s^{-1})	$\langle L_z \rangle$ (kpc km s^{-1})	e	$[L_z^{\max}, L_z^{\min}]$ (kpc km s^{-1})	$\langle L_z \rangle$ (kpc km s^{-1})	e	$[L_z^{\max}, L_z^{\min}]$ (kpc km s^{-1})	$\langle L_z \rangle$ (kpc km s^{-1})
NGC 104	0.17	[1498, 1315]	1397	0.14	[1334, 1298]	1319	0.14	[1342, 1309]	1328	0.16	[1340, 1322]	1332
Pal 1	0.14	[3651, 3637]	3645	0.13	[3648, 3644]	3647	0.13	[3648, 3645]	3647	0.13	[3647, 3645]	3646
NGC 2808	0.86	[471, 445]	458	0.86	[461, 448]	456	0.87	[461, 449]	455	0.86	[471, 451]	461
E 3	0.24	[2259, 2231]	2243	0.24	[2249, 2229]	2240	0.23	[2245, 2235]	2240	0.21	[2242, 2235]	2239
NGC 4372	0.39	[992, 957]	972	0.42	[963, 835]	901	0.38	[964, 936]	951	0.41	[1010, 903]	946
NGC 4833	0.83	[293, 275]	285	0.83	[292, 273]	282	0.83	[290, 263]	277	0.83	[304, 277]	291
NGC 5139	0.68	[−476, −448]	−461	0.67	[−468, −461]	−464	0.67	[−466, −460]	−463	0.67	[−466, −462]	−463
NGC 5927	0.14	[1099, 1073]	1084	0.22	[1315, 1075]	1193	0.13	[1079, 1046]	1066	0.13	[1083, 1064]	1074
NGC 5946	0.87	[147, 126]	137	0.85	[147, 130]	139	0.86	[147, 137]	142	0.86	[152, 132]	142
ES0 224-8	0.20	[3261, 3244]	3253	0.19	[3253, 3245]	3249	0.19	[3249, 3245]	3247	0.19	[3248, 3245]	3247
NGC 5986	0.88	[104, 85]	94	0.86	[105, 89]	96	0.87	[108, 93]	100	0.86	[117, 92]	102
FSR 1716	0.34	[1104, 1061]	1080	0.31	[1121, 1075]	1101	0.31	[1103, 1076]	1088	0.31	[1099, 1071]	1086
BH 184	0.40	[568, 511]	546	0.40	[548, 522]	533	0.44	[591, 485]	543	0.38	[537, 515]	528
NGC 6093	0.81	[31, 21]	26	0.81	[28, 20]	24	0.81	[30, 20]	25	0.78	[37, 25]	31
NGC 6121	0.95	[64, 53]	59	0.95	[63, 52]	59	0.95	[64, 57]	60	0.94	[64, 57]	61
NGC 6144	0.46	[−246, −238]	−241	0.48	[−244, −233]	−239	0.45	[−245, −239]	−242	0.46	[−244, −238]	−241
NGC 6139	0.51	[254, 240]	249	0.48	[254, 240]	247	0.49	[256, 224]	241	0.48	[266, 246]	257
Terzan 3	0.32	[457, 433]	447	0.32	[459, 437]	448	0.37	[509, 426]	470	0.33	[447, 424]	436
NGC 6171	0.51	[196, 184]	191	0.55	[195, 183]	189	0.52	[200, 177]	188	0.50	[206, 184]	195
ESO 452-11	0.90	[−19, −11]	−15	0.90	[−18, −13]	−15	0.90	[−18, −13]	−15	1.00	[−17, −0]	−2
NGC 6218	0.31	[591, 569]	578	0.32	[591, 556]	572	0.31	[611, 574]	594	0.29	[602, 580]	591
FSR 1735	0.95	[−27, −14]	−21	0.93	[−25, −18]	−21	0.94	[−27, −16]	−21	0.92	[−27, −14]	−19
NGC 6235	0.46	[591, 564]	577	0.48	[580, 489]	536	0.47	[575, 555]	566	0.56	[644, 557]	600
NGC 6254	0.39	[611, 590]	598	0.38	[611, 577]	593	0.39	[636, 602]	620	0.38	[620, 602]	610
NGC 6256	0.92	[95, 32]	62	0.89	[88, 75]	81	0.90	[112, 72]	93	0.88	[85, 74]	79
NGC 6266	0.30	[223, 213]	218	0.29	[222, 213]	218	0.29	[226, 214]	220	0.31	[246, 214]	230
NGC 6273	0.80	[−150, −140]	−145	0.80	[−150, −140]	−145	0.81	[−158, −140]	−148	0.81	[−149, −143]	−146
NGC 6287	0.94	[−68, −55]	−60	0.93	[−67, −50]	−59	0.93	[−67, −57]	−62	0.93	[−66, −56]	−60
NGC 6293	0.79	[−98, −88]	−93	0.79	[−96, −89]	−93	0.79	[−108, −90]	−98	0.79	[−96, −90]	−93
NGC 6304	0.30	[488, 472]	482	0.31	[490, 472]	479	0.34	[531, 470]	502	0.31	[478, 437]	458
NGC 6316	0.75	[116, 102]	109	0.74	[114, 103]	107	0.74	[115, 103]	109	0.75	[138, 98]	118
NGC 6325	0.70	[−120, −93]	−105	0.67	[−109, −102]	−105	0.69	[−108, −102]	−105	0.65	[−109, −104]	−107
NGC 6333	0.81	[327, 310]	320	0.81	[328, 318]	322	0.81	[331, 317]	323	0.81	[331, 320]	326
NGC 6342	0.53	[124, 116]	119	0.51	[123, 114]	119	0.52	[125, 115]	120	0.54	[136, 112]	125
NGC 6356	0.50	[738, 706]	721	0.49	[713, 680]	697	0.51	[715, 691]	704	0.49	[730, 707]	719
NGC 6355	0.77	[−100, −88]	−93	0.75	[−97, −89]	−93	0.75	[−100, −91]	−95	0.78	[−97, −91]	−94
NGC 6352	0.23	[812, 759]	783	0.18	[828, 793]	807	0.24	[796, 622]	715	0.16	[795, 774]	786
Terzan 2	0.76	[−49, −44]	−46	0.75	[−49, −44]	−46	0.75	[−48, −44]	−46	0.78	[−49, −43]	−46
NGC 6366	0.42	[714, 690]	700	0.46	[740, 684]	712	0.41	[707, 676]	693	0.41	[703, 685]	693
Terzan 4	0.39	[100, 89]	94	0.35	[95, 89]	92	0.35	[95, 90]	93	0.35	[97, 91]	94
BH 229	0.77	[−25, −18]	−21	0.76	[−26, −19]	−22	0.78	[−24, −19]	−21	0.78	[−25, −18]	−21
NGC 6362	0.31	[599, 579]	587	0.33	[626, 577]	600	0.32	[584, 555]	572	0.32	[585, 568]	577
Liller 1	0.68	[−44, −41]	−42	0.68	[−44, −40]	−42	0.67	[−44, −41]	−42	0.67	[−44, −41]	−42
NGC 6380	0.72	[−106, −96]	−101	0.72	[−106, −99]	−103	0.82	[−109, −93]	−101	0.74	[−107, −99]	−103
Terzan 1	0.61	[104, 93]	99	0.59	[104, 96]	100	0.63	[104, 84]	95	0.59	[104, 96]	100
Pismis 26	0.62	[305, 267]	286	0.63	[287, 269]	277	0.64	[279, 245]	262	0.63	[275, 262]	268

Table A2
(Continued)

Name	$\Omega_{\rm bar} = 31$ km s^{-1} kpc^{-1}			$\Omega_{\rm bar} = 41$ km s^{-1} kpc^{-1}			$\Omega_{\rm bar} = 55$ km s^{-1} kpc^{-1}			$\Omega_{\rm bar} = 70$ km s^{-1} kpc^{-1}		
	e	$[L_z^{\max}, L_z^{\min}]$ (kpc km s^{-1})	$\langle L_z \rangle$ (kpc km s^{-1})	e	$[L_z^{\max}, L_z^{\min}]$ (kpc km s^{-1})	$\langle L_z \rangle$ (kpc km s^{-1})	e	$[L_z^{\max}, L_z^{\min}]$ (kpc km s^{-1})	$\langle L_z \rangle$ (kpc km s^{-1})	e	$[L_z^{\max}, L_z^{\min}]$ (kpc km s^{-1})	$\langle L_z \rangle$ (kpc km s^{-1})
NGC 6388	0.46	[−258, −250]	−253	0.45	[−262, −253]	−257	0.47	[−260, −253]	−256	0.46	[−258, −254]	−256
NGC 6402	0.70	[173, 151]	162	0.68	[163, 151]	157	0.75	[225, 147]	187	0.68	[163, 149]	156
NGC 6401	0.47	[−602, −579]	−590	0.43	[−598, −593]	−595	0.44	[−599, −593]	−596	0.43	[−598, −594]	−596
NGC 6397	0.40	[820, 786]	800	0.40	[861, 762]	807	0.37	[799, 777]	790	0.38	[802, 773]	786
Pal 6	0.91	[61, 46]	54	0.94	[55, 42]	48	0.93	[64, 46]	55	0.93	[56, 48]	52
Djorg 1	0.84	[352, 336]	345	0.85	[353, 341]	347	0.84	[353, 339]	346	0.84	[354, 345]	349
Terzan 5	0.55	[113, 101]	107	0.55	[111, 103]	107	0.60	[111, 86]	98	0.55	[111, 102]	106
NGC 6440	0.68	[−51, −47]	−49	0.69	[−51, −47]	−49	0.68	[−55, −43]	−49	0.69	[−50, −46]	−48
NGC 6441	0.55	[236, 221]	230	0.55	[237, 223]	228	0.56	[236, 216]	226	0.60	[255, 206]	231
Terzan 6	0.76	[−88, −73]	−81	0.76	[−81, −75]	−78	0.76	[−81, −76]	−78	0.86	[−92, −55]	−73
NGC 6453	0.75	[129, 92]	108	0.73	[135, 120]	127	0.73	[133, 99]	118	0.74	[137, 122]	130
NGC 6496	0.50	[1154, 1099]	1125	0.50	[1125, 1102]	1110	0.49	[1134, 1101]	1119	0.48	[1117, 1098]	1107
Terzan 9	0.81	[40, 26]	34	0.82	[34, 27]	31	0.80	[31, 27]	29	0.80	[31, 27]	29
Djorg 2	0.54	[331, 314]	324	0.54	[330, 314]	320	0.56	[342, 313]	328	0.60	[322, 226]	275
NGC 6517	0.82	[141, 113]	130	0.83	[130, 118]	124	0.84	[171, 116]	146	0.81	[131, 117]	124
Terzan 10	0.83	[204, 187]	195	0.81	[201, 184]	192	0.83	[196, 173]	184	0.83	[215, 187]	203
NGC 6522	0.56	[64, 56]	60	0.57	[62, 56]	59	0.57	[63, 56]	59	0.57	[64, 56]	60
NGC 6535	0.62	[−320, −301]	−312	0.64	[−324, −310]	−316	0.63	[−323, −316]	−319	0.62	[−321, −317]	−319
NGC 6528	0.66	[53, 43]	48	0.65	[57, 46]	51	0.66	[54, 45]	49	0.68	[57, 40]	49
NGC 6539	0.32	[351, 336]	345	0.24	[351, 337]	343	0.26	[361, 308]	337	0.23	[364, 343]	354
NGC 6540	0.19	[454, 442]	448	0.19	[456, 439]	446	0.20	[463, 435]	448	0.30	[489, 323]	402
NGC 6544	0.97	[44, 25]	35	0.96	[37, 23]	30	0.96	[36, 26]	31	0.96	[35, 28]	32
NGC 6541	0.56	[364, 334]	346	0.56	[348, 327]	337	0.59	[357, 271]	318	0.56	[342, 326]	334
NGC 6553	0.32	[592, 571]	584	0.31	[602, 580]	590	0.41	[740, 554]	650	0.30	[603, 573]	589
NGC 6558	0.77	[97, 85]	92	0.77	[98, 84]	90	0.75	[98, 86]	92	0.82	[127, 86]	108
Pal 7	0.32	[1046, 1004]	1021	0.33	[1043, 932]	1000	0.31	[1055, 1028]	1045	0.31	[1053, 1019]	1035
Terzan 12	0.32	[680, 606]	641	0.32	[629, 601]	613	0.35	[702, 610]	657	0.32	[641, 620]	632
NGC 6569	0.20	[444, 432]	438	0.19	[447, 432]	438	0.21	[459, 420]	439	0.20	[462, 423]	444
ESO 456-78	0.41	[380, 364]	374	0.40	[386, 369]	376	0.42	[409, 359]	385	0.40	[384, 354]	370
NGC 6624	0.39	[38, 35]	36	0.39	[37, 35]	36	0.39	[37, 34]	36	0.40	[38, 34]	36
NGC 6626	0.61	[175, 163]	170	0.62	[177, 161]	167	0.62	[175, 161]	167	0.69	[226, 138]	179
NGC 6638	0.85	[24, 15]	19	0.86	[28, 17]	23	0.89	[25, 17]	21	0.87	[25, 18]	21
NGC 6637	0.44	[44, 40]	42	0.46	[44, 39]	41	0.47	[44, 40]	42	0.51	[49, 39]	44
NGC 6642	0.85	[42, 26]	34	0.87	[39, 31]	35	0.87	[40, 32]	36	0.87	[38, 30]	34
NGC 6652	0.85	[47, 36]	43	0.86	[49, 39]	42	0.85	[47, 34]	40	0.84	[52, 41]	47
NGC 6656	0.56	[1053, 941]	994	0.56	[1055, 1033]	1045	0.55	[1056, 983]	1018	0.53	[1048, 1032]	1040
Pal 8	0.43	[616, 589]	600	0.44	[621, 587]	603	0.44	[594, 513]	550	0.44	[593, 571]	583
NGC 6681	0.94	[41, 27]	34	0.94	[43, 25]	34	0.94	[52, 23]	37	0.88	[38, 31]	34
NGC 6712	0.89	[108, 91]	99	0.89	[100, 86]	94	0.86	[102, 89]	96	0.85	[98, 90]	94
NGC 6717	0.31	[257, 246]	251	0.27	[251, 237]	245	0.26	[254, 239]	246	0.30	[254, 211]	234
NGC 6723	0.78	[−12, 0]	−4	0.94	[−7, 0]	−1	1.00	[9, −0]	0	0.90	[−25, −0]	−2
NGC 6749	0.46	[701, 555]	634	0.46	[567, 541]	553	0.53	[618, 474]	553	0.46	[570, 549]	561
NGC 6752	0.20	[946, 920]	932	0.26	[1113, 905]	1006	0.19	[938, 912]	925	0.19	[944, 921]	933
NGC 6760	0.40	[743, 712]	724	0.40	[733, 697]	713	0.41	[763, 722]	744	0.40	[746, 718]	727
Pal 10	0.25	[1248, 1209]	1225	0.27	[1315, 1221]	1272	0.25	[1263, 1231]	1244	0.26	[1263, 1182]	1223
NGC 6809	0.71	[268, 251]	260	0.70	[275, 242]	260	0.72	[274, 258]	266	0.71	[272, 259]	266

Table A2
(Continued)

Name	$\Omega_{\rm bar} = 31$ km s^{-1} kpc^{-1}			$\Omega_{\rm bar} = 41$ km s^{-1} kpc^{-1}			$\Omega_{\rm bar} = 55$ km s^{-1} kpc^{-1}			$\Omega_{\rm bar} = 70$ km s^{-1} kpc^{-1}		
	e	$[L_z^{\rm max}, L_z^{\rm min}]$ (kpc km s^{-1})	$\langle L_z \rangle$ (kpc km s^{-1})	e	$[L_z^{\rm max}, L_z^{\rm min}]$ (kpc km s^{-1})	$\langle L_z \rangle$ (kpc km s^{-1})	e	$[L_z^{\rm max}, L_z^{\rm min}]$ (kpc km s^{-1})	$\langle L_z \rangle$ (kpc km s^{-1})	e	$[L_z^{\rm max}, L_z^{\rm min}]$ (kpc km s^{-1})	$\langle L_z \rangle$ (kpc km s^{-1})
Pal 11	0.39	[1062, 1006]	1032	0.37	[1015, 982]	1001	0.37	[1018, 993]	1005	0.37	[1025, 1008]	1018
NGC 6838	0.17	[1443, 1390]	1411	0.17	[1457, 1403]	1435	0.16	[1440, 1417]	1428	0.16	[1434, 1418]	1427
NGC 7078	0.48	[1155, 1109]	1133	0.47	[1138, 1118]	1127	0.48	[1122, 1087]	1107	0.47	[1122, 1100]	1111

ORCID iDs

G. Carraro https://orcid.org/0000-0002-0155-9434

References

Allen, C., & Santillan, A. 1991, RMxAA, 22, 255
Antoja, T., Helmi, A., Dehen, W., et al. 2014, A&A, 563, 60
Bajkova, A. T., & Bobylev, V. V. 2016, AstL, 42, 567
Bajkova, A. T., & Bobylev, V. V. 2017, OAst, 26, 72
Baumgardt, H., Hilker, M., Sollima, A., & Bellini, A. 2019, MNRAS, 482, 5138
Bhattacharjee, P., Chaudhury, S., & Kundu, S. 2014, ApJ, 785, 63
Binney, J., & Tremaine, S. 1987, Galactic Dynamics (Princeton, NJ: Princeton Univ. Press)
Binney, J., & Wong, L. K. 2017, MNRAS, 467, 2446
Bobylev, V. V., & Bajkova, A. T. 2016, AstL, 42, 228
Debattista, V. P., Gerhard, O., & Sevenster, M. N. 2002, MNRAS, 334, 355
Forbes, D. A. 2020, MNRAS, 493, 847
Forbes, D. A., & Bridges, T. 2010, MNRAS, 404, 1203
Gaia Collaboration, Helmi, A., van Leeuwen, F., et al. 2018, A&A, 616, A12
Harris, W. 2010, arXiv:1012.3224
Hernquist, L. 1990, ApJ, 356, 359
Horta, D., Schiavon, R. P., Mackereth, J. T., et al. 2020, MNRAS, 493, 3363
Howard, C. D., Rich, R. M., Reitzel, D. B., et al. 2008, ApJ, 688, 1060
Irrgang, A., Wilcox, B., Tucker, E., & Schiefelbein, L. 2013, A&A, 549, 137
Kunder, A., Koch, A., Rich, R. M., et al. 2012, AJ, 143, 14
Laevens, B. P. M., Martin, N. F., Sesar, B., et al. 2014, ApJL, 786, L3
Mackey, A. D., & Gilmore, G. F. 2004, MNRAS, 355, 504
Massari, D., Koppelman, H. H., & Helmi, A. 2019, A&A, 630, L4
Miyamoto, M., & Nagai, R. 1975, PASJ, 27, 533
Myeong, G. C., Vasiliev, E., Iorio, G., Evans, N. W., & Belokurov, V. 2019, MNRAS, 488, 1235
Navarro, J. F., Frenk, C. S., & White, S. D. M. 1997, ApJ, 490, 493
Ness, M., Freeman, K., Athanassoula, E., et al. 2012, ApJ, 756, 8
Palouš, J., Jungwiert, B., & Kopecký, J. 1993, A&A, 274, 189
Pasetto, E. K., Grebel, T., Zwitter, C., et al. 2012, A&A, 547, A71
Pérez-Villegas, A., Barbuy, B., Kerber, L., et al. 2020, MNRAS, 491, 3251
Piatti, A. E. 2019, ApJ, 882, 98
Plummer, H. C. 1911, MNRAS, 71, 460
Posti, L., & Helmi, A. 2019, A&A, 621, 56
Posti, L., Helmi, A., Veljanoski, J., & Breddels, M. A. 2018, A&A, 615, A70
Sanders, J. L., Smith, L., Evans, N. W., & Lucas, P. 2019, MNRAS, 487, 5188
Schönrich, R., Binney, J., & Dehnen, W. 2010, MNRAS, 403, 1829
Sohn, S. T., Watkins, L. L., Fardal, M. A., et al. 2018, ApJ, 862, 52
Tian, H., Liu, C., Xu, Y., & Xue, X. 2019, ApJ, 871, 184
Vasiliev, E. 2019, MNRAS, 484, 2832
Wegg, C., & Gerhard, O. 2013, MNRAS, 435, 1874
Wilkinson, M. I., & Evans, N. W. 1999, MNRAS, 310, 645
Zinn, R. 1993, in ASP Conf. Ser. 48, The Globular Clusters-Galaxy Connection, ed. G. H. Smith & J. P. Brodie (San Francisco, CA: ASP), 38
Zoccali, M., Gonzales, O. A., Vasquez, S., et al. 2014, A&A, 562, 11